



HAL
open science

Pectin Demethylesterification Generates Platforms that Anchor Peroxidases to Remodel Plant Cell Wall Domains

Edith Francoz, Philippe Ranocha, Aurélie Le Ru, Yves Y. Martinez, Isabelle Fourquaux, Alain Jauneau, Christophe Dunand, Vincent Burlat

► **To cite this version:**

Edith Francoz, Philippe Ranocha, Aurélie Le Ru, Yves Y. Martinez, Isabelle Fourquaux, et al.. Pectin Demethylesterification Generates Platforms that Anchor Peroxidases to Remodel Plant Cell Wall Domains. *Developmental Cell*, 2019, 48 (2), pp.261-276.e8. 10.1016/j.devcel.2018.11.016 . hal-02363268

HAL Id: hal-02363268

<https://hal.science/hal-02363268>

Submitted on 22 Nov 2019

HAL is a multi-disciplinary open access archive for the deposit and dissemination of scientific research documents, whether they are published or not. The documents may come from teaching and research institutions in France or abroad, or from public or private research centers.

L'archive ouverte pluridisciplinaire **HAL**, est destinée au dépôt et à la diffusion de documents scientifiques de niveau recherche, publiés ou non, émanant des établissements d'enseignement et de recherche français ou étrangers, des laboratoires publics ou privés.

Pectin demethylesterification generates platforms that anchor peroxidases to remodel plant cell wall domains

Edith Francoz ^{a,1}, Philippe Ranocha ^{a,1}, Aurélie Le Ru ^b, Yves Martinez ^b, Isabelle Fourquaux ^c, Alain Jauneau ^b, Christophe Dunand ^a, Vincent Burlat ^{a,*}

^a Laboratoire de Recherche en Sciences Végétales, Université de Toulouse, CNRS, UPS, 31326, Castanet Tolosan, France

^b Plateforme Imagerie-Microscopie, CNRS, Université de Toulouse, UPS, Fédération de Recherche FR3450 - Agrobiosciences, Interactions et Biodiversité, 31326, Castanet-Tolosan, France

^c Centre de Microscopie Electronique Appliquée à la Biologie (CMEAB), Faculté de Médecine Rangueil, Toulouse III, Université P. Sabatier, 31062, Toulouse, France

¹ These authors contributed equally to this work

* Correspondence and lead contact: burlat@lrsv.ups-tlse.fr

SUMMARY

Plant cell walls are made of polysaccharidic-proteinaceous complex matrices. Molecular interactions governing their organization remain understudied. We take advantage of the highly dynamic cell walls of Arabidopsis seed mucilage secretory cells to propose a hierarchical multi-molecular interaction model within a cell wall domain. We show that the PECTINEMETHYLESTERASE INHIBITOR6 activity creates a partially demethylesterified pectin pattern acting as a platform allowing positioning of PEROXIDASE36 in a remote primary cell wall domain during early development. This allows triggering the loosening of this domain during later development, in turn leading to proper physiological function upon mature seed imbibition and germination. We anticipate that this pioneer example of molecular scaffold within a cell wall domain is more widespread through other combinations of the individual molecular players all belonging to large multigenic families. These results highlight the role of cell wall polysaccharides-proteins interactions in the organization of cell wall domains.

INTRODUCTION

Plant cell walls are complex matrices whose dry mass is primarily made of about 90% polysaccharides (cellulose microfibrils, hemicelluloses and pectins) and about 10% of cell

wall proteins (Albenne et al., 2014). In specialized cell types, they may encompass additional hydrophobic polymers such as lignins, cutin, sporopollenin or suberin. Plant cell walls are heterogeneous and dynamic structures since their composition varies all along plant development and in response to environmental changes, within plant species, organs, cell types and cell wall sub-layers or polarized patches within the wall that we hereafter name cell wall domains (Lee et al., 2011; Popper et al., 2011; Seifert and Blaukopf, 2010). Current architectural models attempt at assembling these molecular components in simple types of wall categories distinguished either with an evolutionary perspective (*e.g.* monocots vs dicots walls) or with cellular and developmental considerations (*e.g.* primary vs secondary walls) (Busse-Wicher et al., 2016; Popper et al., 2011; Carpita and Gibeaut, 1993). The development of molecular tools such as specific antibodies against wall components (*e.g.* polysaccharides, lignins, cell wall proteins) enabled illustrating that, except cellulose, which is a universal component, each cell type is surrounded by a particular wall and thus exhibits its own specific set of wall epitopes (Hall et al., 2013; Lee et al., 2011; Burlat et al., 1997). While looking more closely at a given cell type, the wall epitope distribution often follows layers, patches or polarized deposition illustrating the ultrastructural complexity of a given cell wall. The term “cell wall microdomain” has been previously proposed to describe such discrete topochemical organization (Willats et al., 2001). However, the understanding of the specific molecular interactions within these polarized domains and the resulting functions remain limited (Lee et al., 2018; Lee et al., 2013; Roppolo et al., 2011).

During plant seed development, some of the most dramatic changes occur within the epidermal cell walls, with major impacts on seed dormancy and germination (Francoz et al., 2015a). The ‘myxospermy’ phenomenon consists in the accumulation of large amounts of pectic cell wall-like structures called mucilage in the seed epidermis of various angiosperm species (North et al., 2014; Western, 2012). The seed coat epidermal cells also called mucilage secretory cells (MSCs), constitute a fascinating single cellular model for multiple plant cell wall domain dynamics (Francoz et al., 2015a). MSCs successively produce three kinds of walls (i) a primary wall surrounding the cell, (ii) an internal mucilage and (iii) an internal secondary wall (columella) compacting the mucilage towards the outer periclinal primary wall. Upon dry seed imbibition, the outer primary wall is locally ruptured, thus allowing the release of a mucilage crown constituting a hydrogel surrounding the seed and influencing seed dispersion and germination (Western, 2012). Among the *circa* 60 proteins known to be involved in MSC dynamics in *Arabidopsis thaliana* (Francoz et al., 2015a), PECTIN METHYLESTERASE INHIBITOR6 (PMEI6) and PEROXIDASE36 (PRX36) are

two separately studied cell wall proteins whose mutants display a similar phenotype of delayed mucilage release due to reinforcement of the polarized rupture wall domain (Ranocha et al., 2014; Kunieda et al., 2013; Saez-Aguayo et al., 2013). This raises the question on whether and how these two proteins could work together. They are both encoded by multigenic families: *Pectin methylesterase inhibitors (PMEIs)* (Scheler et al., 2015) and *class III peroxidases (CIII PRXs)* (Francoz et al., 2015b). Conceptual speculated molecular intermediates between these two types of cell wall proteins could be homogalacturonan (HG) pectic domains.

HGs vary in size (polymers of $\alpha(1-4)$ -linked galacturonic acid moieties with various degrees of polymerization), and in charge (various patterns of methylation enabling the neutralization of selected galacturonic acid negative charge). HGs are synthesized in the Golgi apparatus and the galacturonic acid carboxyl residues are neutralized by methylesterification prior to be exported to the cell wall (Driouich et al., 2012; Mouille et al., 2007). In the wall, PMEIs are proteins that interact in a 1:1 ratio with pectin methylesterases (PMEs) (Scheler et al., 2015) to fine-tune PME activity and, as a consequence to regulate the degree of methylesterification of HG within the wall (Jolie et al., 2010; Wolf et al., 2009). PMEs/PMEIs control the recovery of the negative charge of selected galacturonic acids by releasing specific HG methyl groups and therefore impact cell wall physicochemical and mechanical properties by controlling the ‘egg-box’ calcium-pectate formation (Carpita and Gibeaut, 1993). HGs, PMEs and PMEIs have already been localized to cell wall domains with missing explanation for all this complex spatio-temporal distribution (Peaucelle et al., 2015; Saez-Aguayo et al., 2013; Willats et al., 2001; Morvan et al., 1998). In addition to the PMEs/PMEIs concerted action, CIII PRXs also contribute to the cell wall dynamics through their dual catalytic cycle, allowing either wall loosening (Schweikert et al., 2000; Fry, 1998) or wall stiffening (Schopfer, 1996), and may play signaling role by controlling reactive oxygen species homeostasis (Francoz et al., 2015b; Gadjev et al., 2006). Similarly to HGs/PMEs/PMEIs, CIII PRXs have been localized to polarized wall domains in relation with their specific cell wall remodeling functions (Kunieda et al., 2013; Lee et al., 2013). Either transmembrane proteins (Lee et al., 2013) or HGs (Passardi et al., 2006; Shah et al., 2004; Carpin et al., 2001) have been proposed to directly or indirectly allow anchoring of CIII PRXs to cell walls. However, no formal wall domain molecular scaffolds were shown between individual HG, PME, PMEI, CIII PRX and transmembrane proteins.

In the present work, using a combination of reverse genetics, molecular and cell biology, computational molecular modeling and biochemistry, we demonstrate that the specific HG

demethylesterification pattern controlled by PME16 within a MSC outer periclinal wall domain acts as a platform necessary for PRX36 specific anchoring to this wall domain, consequently enabling previously proposed restriction of wall loosening to this domain (Kunieda et al., 2013). We partially identified the HG specific methylesterification pattern and PRX36 amino acids responsible for the interaction within the wall domain further enabling the PRX36 restricted loosening function. We propose a spatio-temporal model of sequential action of PME16 and PRX36 explaining the similar abnormal seed mucilage release phenotype of *pmei6* and *prx36* mutants from the macroscopic to the ultrastructural scale, and discuss how the established molecular relationship may constitute a proof of concept paving the way for the discovery of future similar interactions along plant development and in response to the environment changes.

RESULTS

The relationship between PRX36 and PME16 is at the protein accumulation level rather than at the gene expression regulation level

The rationale of this study was based on two observations. First, *PRX36* and *PME16* are highly co-expressed during *A. thaliana* seed development according to publicly available tissue-specific transcriptomic data (Belmonte et al., 2013). The seed coat-specific expression of both genes starts at linear cotyledon stage (7-8 day after pollination (DAP)), and gradually decreases afterward (Figure 1A). It is remarkable that within the *PRX36* co-expression network built with this dataset, *PME16* is the first hit with a Pearson correlation coefficient of 0.9474 indicating that these two genes are the most closely co-expressed (Figure 1B). The laser-captured seed coat samples used for the transcriptomic analysis encompass five cell layers (Belmonte et al., 2013), but both genes are expressed only in the outermost MSC layer (Francoz et al., 2016; Kunieda et al., 2013; Saez-Aguayo et al., 2013). Second, a similar abnormal mucilage release phenotype has been described for *prx36* and *pmei6* knock-out mutants (Kunieda et al., 2013; Saez-Aguayo et al., 2013). We first confirmed this common phenotype. Seeds stained with ruthenium red without shaking show no pink red mucilage release for both mutants as compared to the Col-0 control (Figure 1C-H). Seeds vigorously shaken in water show a similar abnormal peeling of MSC outer cell wall in both mutants (Figure 1I-N).

We next investigated *PRX36* and *PME16* expression level during seed development of Col-0, *prx36-1* and *pmei6-1* (Figure S1A). In Col-0, *PRX36* is expressed at 6 and 7 DAP while *PME16* expression lasts from 5 to 14 DAP with the highest expression levels at 7 and 8 DAP,

in agreement with previous work (Belmonte et al., 2013; Kunieda et al., 2013; Saez-Aguayo et al., 2013). The absence of *PRX36* and *PMEI6* expression in the corresponding mutants (Figure S1A) confirms their knocked out status (Kunieda et al., 2013; Saez-Aguayo et al., 2013). Since CIII PRXs, and pectin modifying enzymes may have signaling roles (Francoz et al., 2015b; Gadjev et al., 2006; Dumville and Fry, 2000), it is interesting to observe that *PRX36* and *PMEI6* expression profiles are not affected in *pmei6-1* and *prx36-1*, respectively. These results suggest that *PRX36* has no direct signaling role on *PMEI6* expression and *vice versa*.

We raised α PRX36 antibodies to perform comparison at the protein level (Figure S1B). Faint non-specific signal is visible in all samples at the position of abundant proteins such as RUBISCO. Two PRX36-specific bands (absent in *prx36-1*) at 39.8 kDa and 46.8 kDa appear in Col-0 at 6 DAP and peak at 8 and 10 DAP. At 12 and 14 DAP only the 39.8 kDa band is observed in good agreement with the theoretical molecular mass of the mature protein (38.2 kDa for the full sequence and 35.2 kDa without the 3 kDa predicted signal peptide and without considering putative glycosylation). The presence of two PRX36-GFP-specific bands at early stages was previously reported (Kunieda et al., 2013) even if the delta was different between both studies (7 kDa in Figure S1B vs 3 kDa in Kunieda et al., 2013). These differences could be due to *N*-glycosylation (predicted site at N234) and/or *O*-glycosylation (five Pro residues P51, P131, P154, P178, P179 could be hydroxylated in hydroxyproline residues as already described for other CIII PRXs (Nguyen-Kim et al., 2016)). Besides, one cannot exclude some protein degradation. However, contrary to the previous study that did not detect any PRX36-specific bands after 10 DAP (Kunieda et al., 2013), we observe the 39.8 kDa band at all the later stages studied. This is consistent with the recent identification of PRX36 in a mucilage cell wall proteome from imbibed mature seeds (Tsai et al., 2017). Interestingly, in *pmei6-1*, the two PRX36 bands are observed at 8 DAP and somehow at 10 DAP, but disappear at later stages. Altogether, even if we cannot exclude a complex unidentified compensation phenomenon, the most plausible scenario deduced from these results suggests that the stable accumulation of the PRX36 protein along seed developmental kinetics indirectly relies on the *PMEI6* enzymatic activity, providing a first possible temporal and hierarchical relationship between these two proteins.

The homogalacturonan methylesterification pattern controlled by *PMEI6* is necessary for *PRX36* stable anchoring to its cell wall domain

We hypothesized that the HG methylesterification pattern finely tuned by an unknown PME under the control of *PMEI6* could enable PRX36 anchoring to its cell wall domain. We used previously generated *proPRX36:PRX36-GFPg4/prx36-1* plants (Kunieda et al., 2013) to challenge this assumption. We monitored the fluorescence emitted by the fusion protein in young developing seeds (about 7 DAP) following chemical treatments modifying HG physico-chemical properties (Figure 2). We used sodium phosphate buffer as a negative control, Na_2CO_3 as a HG demethylating solution to evaluate the role of methylesterified residues (Singh et al., 2009) and EDTA as a calcium chelating agent therefore dissociating the calcium-demethylated HG “egg-box” structure. Before treatments, the maximum projection of Z stacks and corresponding orthogonal views (Figure 2A, C, E, columns 1-3) show that the GFP fluorescence emitted by PRX36-GFPg4 is localized to the cell wall domain corresponding to the boundary between the radial and outer primary walls (Kunieda et al., 2013). This fluorescence pattern surrounds the mucilage, in turn surrounding the amyloplasts positioned in the zone where the columella will eventually be assembled (Figure 2, A, C, E, columns 2-4). Semi-quantitative analysis shows that the trans-cellular fluorescence profile is overall reproducible before treatments (Figure 2A, C, E, column 5). Both HG-modifying treatments rapidly lead to a mislocalization of the fluorescence from the primary wall domain toward the underlying mucilage surrounding the intracellular amyloplasts (Figure 2D, F). As a control, no such delocalization occurs in seeds treated with sodium phosphate buffer indicating that the delocalization is not due to the osmotic properties of the solutions but rather to their chemical effects (Figure 2B). The fact that both Na_2CO_3 (acting on methylesterified moieties) and EDTA (chelating Ca^{2+} interacting with negatively charged moieties) lead to delocalization patterns suggests that PRX36 anchoring necessitates a peculiar HG structure with a partial methylesterification pattern. The overall morphology of the cells does not appear to be impacted by the treatments since the amyloplast distribution is conserved (Figure 2, column 4). However, the whole seed view and the semiquantitative analysis show that the delocalized fluorescence pattern does not occur in all the cells, possibly due to heterogeneous infiltration efficiency of the solutions among the cells.

To progress in the understanding of the cause of this delocalization, we tested the localization pattern of PRX36 in the *pmei6-1* genetic background. Since the Western blot analysis indicated that the endogenous PRX36 was stably accumulating along Col-0 seed development (Figure S1B) whereas the *proPRX36:PRX36-GFPg4/prx36-1* line showed a transient PRX36-GFPg4 localization at early developmental stages (Kunieda et al., 2013), we generated *proPRX36:PRX36-TagRFP* lines. Indeed, TagRFP is a low pKa fluorescent protein

particularly adapted to the acidic environment of plant cell walls (Albenne et al., 2014). In the Col-0 background, the time course series along seed development kinetics show a stable fluorescence of the TagRFP fusion protein within the cell wall domain of MSCs (Figure 3A). We used this cell wall-adapted reporter to transform *prx36-1* and *pmei6-1* mutants as well as the corresponding double mutant. The comparison of the PRX36-TagRFP fluorescence in Col-0 and *prx36-1* control backgrounds shows a faint partial mislocalization to the mucilage at 12 DAP in Col-0, whereas the fluorescence is restricted to the cell wall domain in *prx36-1* (Figure 3A). This suggests a partial competition between the endogenous PRX36 and exogenous PRX36-TagRFP at late developmental stages in Col-0 background. Comparison of the PRX36-TagRFP localization in Col-0 and *pmei6-1* shows a marked mislocalization toward the mucilage starting at 7-8 DAP and spreading to the columella-mucilage boundary at 10-12 DAP. This difference is even more pronounced when comparing PRX36-TagRFP localization in *prx36-1* vs. *prx36-1* × *pmei6-1* allowing circumventing the competition between PRX36-TagRFP and the endogenous PRX36 at later stages (Figure 3A). The relative fluorescence intensity profiles at 12 DAP clearly highlight the mislocalization of PRX36-TagRFP observed in the lines harboring the *pmei6-1* mutation (Figure 3A, B). This result is in agreement with the mislocalization of PRX36-GFP following HG-modifying chemical treatments (Figure 2) and with the disappearance of PRX36 in *pmei6-1* after 8 DAP probably due to the degradation of the mislocalized protein (Figure S1B).

To confirm these results, we localized the endogenous PRX36 with α PRX36 on sections of paraffin-embedded tissue microarrays of seed development kinetics from Col-0, *prx36-1* and *pmei6-1* (Figure 4). Consistently with the presence of unspecific RUBISCO-like bands on Western blots, some unspecific labeling is detected in the embryo of all genetic background/developmental stages, as exemplified with Col-0 and *prx36-1* (Figure S2A, D). This does not impair the visualization of the cell wall domain-dotted PRX36 pattern all around the seed coat, specific to Col-0 as compared to *prx36-1* (Figure S2A, D). This pattern could be observed from 8 DAP up to 12 DAP (Figure 4B). No such signal is visible along the *prx36-1* seed developmental kinetics, confirming the labeling specificity at the outer wall domain position (Figure 4B). This labeling is also lost in *pmei6-1* in agreement with our previous results indicating that in absence of the HG pattern controlled by PME16, the endogenous PRX36 is unable to be anchored to its cell wall domain and that the mislocalized enzyme is most likely degraded (Figure 4B).

The PME16-specific partially methylesterified homogalacturonan LM20 and JIM7 epitopes are necessary for PRX36 anchoring to the functional cell wall domain

In an attempt at identifying the HG methylesterification pattern controlled by PME16 activity and necessary for PRX36 anchoring, we screened commercially available HG-specific antibodies in double immunofluorescence labeling with PRX36 antibodies on serial sections from paraffin-embedded tissue microarrays. The specificity of the secondary markers for the rabbit α PRX36 and the rat JIM and LM antibodies is first assessed (Figure S2G-Z).

Interestingly, LM20 (Figure 4) and to a lower extent JIM7 (Figure S3), two antibodies specific to partially methylesterified HG (Verhertbruggen et al., 2009; Clausen et al., 2003) colocalize with α PRX36 in the cell wall domain along the wild-type seed development kinetics. The labeling of LM20 (Figure 4) and JIM7 (Figure S3) epitopes is conserved in *prx36-1* but lost in *pmei6-1*. On the one hand, the conservation of LM20/JIM7 epitopes in *prx36-1* suggests that these HG motifs are not the substrate of PRX36. On the other hand, the loss of the three epitopes (PRX36 and LM20/JIM7) in *pmei6-1* indicates that the partially methylesterified HG epitopes are related to PME16 activity and that these HG patterns are probably necessary for PRX36 anchoring. Moreover, the loss of LM20/JIM7 epitopes in *pmei6-1* occurs at 8 DAP suggesting that the PME16 activity started at this stage, shortly after the onset of *PME16* expression (Figure S1A). It has to be noticed that the spatial colocalization of LM20/JIM7 and PRX36 epitopes is not absolute during the developmental kinetics. Indeed, PRX36 epitopes are more readily observed at earlier stages of development while, LM20/JIM7 epitopes are most clearly observed before PRX36 detection and at later developmental stages after PRX36 disappearance. In *prx36-1*, JIM7/LM20 epitope detection is more stable along the kinetics. It is tempting to speculate that this could be related to the proximity of both epitopes leading to limitation of accessibility to both antibodies at the same time.

The theoretical spatial resolution of Alexa fluor 488 fluorescence in confocal microscopy corresponds to a xyz environment of 161 nm \times 161 nm \times 574 nm in our conditions (see STAR methods for details). This illustrates that the colocalized fluorescence signals could be either juxtaposed or positioned anywhere within this spatial environment. At the intermediate stages when both epitopes better colocalize, we took advantage of this double immunofluorescence labeling to increase the spatial resolution and assess the proximity of LM20/JIM7 and PRX36 epitopes using a fluorescence resonance energy transfer (FRET) approach of double immunofluorescence signals (Konig et al., 2006) coupled to fluorescence lifetime imaging microscopy (FLIM), adapting the recently described state-of-the-art FRET-FLIM technology

(Camborde et al., 2017). The comparison of the mean lifetime (τ) of the FRET donor (α PRX36/A488 nm) in absence and presence of potential FRET receivers (LM20/A555 nm or JIM7/A555) shows a variation of the mean lifetime ($\Delta\tau$) of 238 ps or 200 ps with a p -value of $1.3 \cdot 10^{-13}$ or $4.2 \cdot 10^{-10}$, respectively, indicating the statistical significance of the FRET (Figure 5). The Gaussian repartition of the individually measured lifetimes for each of the 30 regions of interest enables calculating a donor-acceptor Förster distance of 10.16 nm for α PRX36-LM20 and 10.49 nm for α PRX36-JIM7 immunocomplexes. These experimental distances correspond to a FRET efficiency of about 10% which can be considered as the sign of the interaction of both fluorochromes (Camborde et al., 2017). Even if this result does not formally prove the molecular interaction of the epitopes given the size of the immunocomplexes, it provides an experimental evidence of the physical proximity of LM20/JIM7 and PRX36 epitopes *in muro* at a nanometer scale. This result is strengthened by a negative control using xyloglucan-specific LM25 antibody which also colocalizes with PRX36 immunolabeling (Figure 5). The $\Delta\tau$ is reduced to 19 ps with no statistical significance (p -value = 0.356) reinforcing the demonstration of the proximity of α PRX36-JIM7/LM20 partially methylesterified HG epitopes rather than those of α PRX36/LM25 xyloglucan epitopes. We also took advantage of CBM3a that labels crystalline cellulose to perform FRET-FLIM analysis of either α PRX36, JIM7 or LM25 immunocomplexes *vs.* CBM3a cellulose immunocomplex colocalizing in the outer wall domain (Figure S4). No FRET occurs for α PRX36/CBM3a double labeling providing an additional negative control for α PRX36 (Figure S4A-C). Similarly, no FRET is observed for JIM7/ CBM3a providing a negative control for JIM7 (Figure S4D-F), while a clear FRET is observed for LM25/CBM3a constituting a positive control for xyloglucan/cellulose-specific immunocomplexes (Figure S4G-I). Therefore FRET-FLIM double immunofluorescence provides additional clue towards a specific molecular interaction/proximity between PRX36 and the PME16-specific partially methylesterified HG patterns recognized by LM20/JIM7 within the MSC outer cell wall domain.

***In silico* identification and *in vivo* functional validation of PRX36-specific amino acids necessary for homogalacturonan binding and PRX36 function**

We built a PRX36 model based on PRX53 crystallographic data (Ostergaard et al., 2000) and used it to perform *in silico* docking experiments with the five hexagalacturonates tested for the competitive inhibition characterization of JIM7 specificity (Clausen et al., 2003) (Figure

S5). Unfortunately, no such information is available for LM20 (Verhertbruggen et al., 2009). This *in silico* approach enables identifying a valley on PRX36 surface where most of the hexagalacturonates are predicted to bind. We observe a better specificity for the 3 hexagalacturonates displaying the highest specificity for JIM7 (Figure S5A-D). It should be noted that this PRX36 valley is distal from the epitope used for the α PRX36 antibody production (Figure S5C) in agreement with our ability to simultaneously label PRX36 and JIM7 epitopes *in situ* (Figure 5; Figure S3). Since the PRX36 model does not take into account the post-translational modifications (PTMs) that could be important for PRX36-HG interactions, we have highlighted the putative sites of N- and O-glycosylation (Figure S6E). These amino acids are located in distal parts of the protein as compared to the predicted hexagalacturonate docking valley indicating that the docking prediction is not likely to be impaired by distant putative PTMs.

We choose the hexagalacturonate (oo888o) which displayed the best affinity for JIM7 (Clausen et al., 2003) and the best docking predictions on the PRX36 valley (Figure S5) to progress on the understanding of this predicted interaction. We first identified the 26 amino acids present in a 5 Å environment around the 8 best *in silico* HG docking models defining the predicted docking valley (Figure S6A). We next highlighted the 6 polar positive and 2 hydrophobic amino acids, since these amino acid categories were reported to be involved in CIII PRX binding to negatively charged HG (Passardi et al., 2006; Shah et al., 2004; Carpin et al., 2001), and in protein binding to neutral sugars (Sujatha et al., 2004), respectively (Figure S6B). Finally, we extended this selection list by adding 4 residues (R214, R219, R339 and Y261) surrounding the 5 Å environment (Figure S6C). *In silico* demonstration of the importance of these amino acids was performed using PRX50 (co-expressed with PRX36 within the MSCs (Francoz et al., 2016) but sharing only 32 % amino acid identity with PRX36) and PRX36m (displaying site-directed mutagenesis on 6 polar and 2 hydrophobic amino acids from the predicted binding valley) (Figure S6D-G). The specific HG docking prediction observed with PRX36 is completely lost with PRX50 and partially lost with PRX36m. In addition, PRX36m shows a shift as compared to PRX36 in the alignment of HG models along a virtual axis materializing alternate polar positive and hydrophobic amino acids inside the predicted binding valley (Figure 6A; Figure S6F). In order to provide functional validation of this *in silico* approach, we constructed *proPRX36:PRX-TagRFP* lines for PRX36, PRX50 and PRX36m in the *prx36-1* background (Figure 6B-F). The dual goal of this approach was to assess whether the *in silico* docking prediction (Figure 6A) was in agreement with the ability of the fusion protein (i) to localize to the cell wall domain along the seed

developmental kinetics (Figure 6C) and (ii) to restore a wild-type mucilage release phenotype at mature stage (Figure 6D-F). While the *prx36-1* lines expressing PRX36-TagRFP display a stable cell wall domain localization of PRX36-TagRFP allowing to restore the wild type mucilage release phenotype, neither PRX50-TagRFP nor PRX36m-TagRFP expressing lines allow achieving the same result (Figure 6C, D). PRX50-TagRFP is localized to the mucilage whereas PRX36m-TagRFP enters the secretory pathway as previously reported for the non mutated fusion protein (Kunieda et al., 2013), but quickly disappears from the MSC. In addition, none of these lines is able to complement the *prx36-1* phenotype (Figure 6C, D). Quantitative analysis of mucilage area and mucilage circularity on about 200 seeds and heatmap color representation of the results show the clear-cut results among all the tested lines (Figure 6E, F). None of the mutated amino acids is located in the predicted signal peptide (Figure S6D). However, to ensure that the mislocalization of PRX36m-TagRFP was not related to an inability to reach the cell wall, we show the cell wall localization of both PRX36-TagRFP and PRX36m-TagRFP when overexpressed in *N. benthamiana* (Figure S7A, B). None of the mutated amino acids corresponded to the 6 consensus amino acids necessary for heme binding (Mathé et al., 2010) (Figure S6D). R110G was proximal to N109 but without impairing the catalytic activity since PRX36-TagRFP and PRX36m-TagRFP transiently overexpressed in *N. benthamiana* show a similar CIII PRX activity (Figure S7C). The means by which PRX36m-TagRFP disappears from MSCs is unknown but it could be related to proteolysis of the mislocalized protein. The mislocalization of PRX36 occurring when the pectin platform is impaired is more pronounced with immunological approaches than with genetic approaches (Figures 2, 3, 4, S1, S3), and less pronounced than the mislocalization occurring with site directed mutagenesis (Figure 6). This may be due either to differences in relative sensitivity of the detection methods or could suggest unidentified additional factor(s) necessary for anchoring PRX36 to its cell wall domain. However, the *in silico* prediction is strikingly validated by this dual localization/functional approach. *proPRX36*-driven expression of PRX50-TagRFP or PRX36m-TagRFP in *prx36-1* does not allow to localize the fusion protein to the cell wall domain, neither to complement the mucilage release phenotype. Only PRX36-TagRFP allows achieving this dual goal, pointing out to the crucial role of the anchoring of the fusion protein to reach its proper functional role.

Ultrastructural dry seed MSC microphenotyping

The ruthenium red mucilage release phenotyping is performed on imbibed mature dry seeds (Western, 2012), but it is challenging to observe the ultrastructure of the outer wall domain itself just before release. We set up an original protocol allowing circumventing this problem (see STAR Methods for details). The transmission electron microscopy observation shows naturally-different electron density among the three types of MSC walls that are highlighted by false colors (Figure 7A). No differences are observed between the three genotypes for the volcano-shaped secondary wall constituting the columella and the dry mucilage compacted between the columella and the primary wall. However, comparison of close-up views from the outer / radial primary wall junction constituting the studied PME16-HG-PRX36 domain reveals a thinning in Col-0 and a thickening in *prx36-1* and *pmei6-1* (Figure 7A). Assuming that electron density is directly correlated to cell wall density, the cell wall domain thinning could correspond to localized wall loosening produced by the PRX36 activity during the wild type seed development (Kunieda et al., 2013), whereas the more electron dense cell wall domain observed in the mutants is consistent with an absence of loosening when either PRX36 is not expressed (*prx36-1*) or PRX36 is not correctly anchored to the cell wall domain (*pmei6-1*). In both cases, the more resistant cell wall domain leads to the observed delay in mucilage release.

DISCUSSION:

Spatio-temporal ultrastructural model of the functional organization of the PME16-HG-PRX36 molecular scaffold cell wall domain

Our results shed light on the combinatory actions of two cell wall proteins sequentially participating to the loosening of a cell wall domain during seed development that is crucial for proper mucilage release upon dry seed imbibition days-to-years later after mature seed desiccation (Figure 7B, C). First, our results indicate that PME16 controls during seed development a yet to be discovered PME in order to generate a peculiar HG methylesterification pattern recognized by JIM7/LM20 antibodies in the cell wall domain. Then, this amphiphilic polysaccharidic platform allows the specific anchoring of PRX36, enabling loosening the cell wall domain later during seed development. We identified at the PRX36 surface a HG binding valley through *in silico* analysis and provided a first *in vivo* validation of the importance for PRX36 anchoring of some polar and hydrophobic amino acids exposed at the valley surface. In turn, we show that the localized positioning of PRX36 is necessary for the tightly controlled wall loosening at the future weakened positions that will be ruptured upon seed imbibition. Our results shed light on possible protein-polysaccharide

interaction that were not identified in other cell wall domain recent examples (Lee et al., 2018; Lee et al., 2013; Roppolo et al., 2011). So far, CIII PRX binding to HGs implicated calcium-mediated interaction on negatively charged demethylated HGs and were neither related to the PME/PMEI-dependent fine tuning of HG demethylesterification, nor to a direct physiological function (Passardi et al., 2006; Shah et al., 2004; Carpin et al., 2001). Conversely, pectin-CIII PRX interaction has long been purported during lignin polymerization, but without formal study of the molecular scaffold (Warinowski et al., 2016; Wi et al., 2005). Our results propose a docking role to a partially methylesterified HG acting as an anchoring platform. There are at least four important significances for these results. First, we propose that the accurate positioning of a CIII PRX to its exact site of action constitutes a means to target its specific action. Indeed, CIII PRXs usually oxidize a wide range of substrates *in vitro* whereas the *in vivo* specificity relies on their co-localization with substrates in their close micro-environment, such as cell wall domains (Francoz et al., 2015b; Kunieda et al., 2013; Lee et al., 2013). The horseradish peroxidase (HRP) is the best example to illustrate this particularity since this vacuolar CIII PRX is able to convert a wide range of chromogenic substrates *in vitro* contributing to its use by scientists as a popular enzymatic marker for immunological assays. In addition, HRP is also able to polymerize aromatic substrates such as monolignols to produce *in vitro* lignin-like oligomers (Mechin et al., 2007) that are not its *in vivo* natural products considering the spatial separation of the vacuolar HRP from the wall-localized lignins (Matsui et al., 2003). This peculiarity of CIII PRXs relies on their ability to produce reactive oxygen species (ROS) that in turn activate the substrates present in their surrounding micro-environment and does not necessitate a direct specific binding to their substrate (Francoz et al., 2015b). Here, we propose that PRX36 binding to a specific polysaccharidic motif considered as an anchoring platform, and not as an enzymatic substrate, could be a means to target the CIII PRX *in muro* activity towards co-localized potential substrates yet to be identified.

Second, the biological significance of this result is illustrated while considering the temporal dimension in addition to the spatial dimension of the process (Figure 7C). The stable accumulation of PRX36 along seed development makes sense while considering both the modification of the position of the plasma membrane during MSC maturation, and the wall loosening function of PRX36. PRX36 positioning in its cell wall domain is facilitated by the vicinity, at early MSC developmental stages, of the primary wall and the plasma membrane as the end-point of the secretory pathway used for protein targeting to the cell wall. Indeed, at later stages (*e.g.* 12 DAP), the positioning of PRX36 in its cell wall domain would be

probably impaired by the distance to the plasma membrane due to the interposed mucilage (Figure 7C). In turn, considering the proposed loosening function of PRX36 (Kunieda et al., 2013), a premature cell wall domain weakening before the end of MSC expansion and wall production would probably be detrimental for the cell integrity. We rather assume that the early production and stable accumulation of PRX36 is necessary to enable the late cell wall domain loosening activity when all the wall synthesis and cell expansion processes are completed. This spatio-temporal model also considers the catalytic cycle of CIII PRXs that necessitate a triggering pool of H₂O₂ produced by active members of the NADPH oxidase (RBOH) and superoxide dismutase (SOD) multigenic families. These enzymes could be far from the cell wall domain given their subcellular localization and the long-distance diffusion capacity of H₂O₂ (Barcelo, 2005). The identification of RBOH and SOD isoforms necessary for PRX36 activity and the determination of their spatio-temporal localization pattern will be crucial.

Third, there are of course some missing molecular players in our model. The most obvious one is the PME controlled by PME16. One candidate could be a PME named HIGHLY METHYL ESTERIFIED SEEDS whose mutant presents a mucilage release defect phenotype similar to those of *pme16-1* and *prx36-1* (Levesque-Tremblay et al., 2015a). Recent examples have shown how specific PME/PMEI couples finely tune the methylesterification pattern of HGs in other developmental contexts (Levesque-Tremblay et al., 2015b; Sénéchal et al., 2015). Moreover, considering the beginning of the assembly of the cell wall domain molecular scaffold, we can expect that a plasma membrane protein such as *e.g.* a member of the CASPL multigenic family (Roppolo et al., 2014) could initiate the molecular scaffold as proposed for the positioning of PRX64 in the root endodermis Casparian strips that actually constitute another cell wall domain necessitating a localized CIII PRX stiffening activity (Lee et al., 2013; Roppolo et al., 2011). Interestingly, no physical interaction was demonstrated between CASP1 and PRX64 rising the question of whether a missing piece could be another combination of PME/PMEI/HG.

Finally, we postulate that this example of cell wall domain molecular organization should find counterparts in the future in other cell wall domains of MSCs as well as other cell types and other plants. This is supported by the similarly sized multigenic families of the presently identified molecular players with about 70 members in *A. thaliana* for each *PME*, *PMEI*, *CIII PRX* (Francoz et al., 2015b; Scheler et al., 2015) and the 64 theoretical methylesterification combinations for a hexagalacturonate fitting to the PRX36 binding valley. This also raises the question of a possible co-evolution of these multigenic families in the green lineage together

with the cell wall complexity. Concerning the MSCs, other *PMEs*, *PMEIs* and *CIII PRXs* are expressed during seed coat development and may be part of functional loosening/stiffening of additional cell wall domains within this cell type example (Shi et al., 2018; Francoz et al., 2016; Turbant et al., 2016; Belmonte et al., 2013). Consequently, within MSCs as well as more generally in any cellular contexts, fully integrating the cell wall domain and interaction angles to future cell wall protein and polysaccharide functional studies seems highly relevant.

ACKNOWLEDGMENTS

We thank the Paul Sabatier Toulouse 3 University and the *Centre National de la Recherche Scientifique* (CNRS) for granting this work. This work was also supported by the French Laboratory of Excellence project "TULIP" (ANR-10-LABX-41; ANR-11-IDEX-0002-02) and the French National Research Agency project "MicroWall" (ANR-18-CE20-0007). We are grateful to H. North (IJPB, Versailles, France) and I.-H. Nishimura (Kyoto University, Japan) for providing seeds, and to P.-M. Delaux (LRSV, Auzeville, France) for the gift of pL2V-Hyg and helpful discussions about Golden Gate cloning. We also thank H. San Clemente, M. Aguilar and M. Bonhomme (LRSV, Auzeville, France) for help using Microsoft Excel and R commands. Thanks are extended to C. Pouzet (Toulouse Imaging platform) and E. Jamet (LRSV, Auzeville, France) for confocal microscopy and critical comments on the manuscript, respectively.

AUTHOR CONTRIBUTIONS

Conceptualization, C.D. and V.B.; Methodology, all authors; Investigation, E.F., P.R., A.J. and V.B.; Writing – Original Draft, V.B.; Writing – Review & Editing, P.R., C.D. and V.B.; Funding Acquisition, C.D. and V.B.; Resources, E.F., P.R., C.D. and V.B.; Supervision, C.D. and V.B.

DECLARATION OF INTERESTS

The authors declare no competing interests.

REFERENCES

- Albenne C., Canut H., Hoffmann L., and Jamet E. (2014). Plant cell wall proteins: a large body of data, but what about runaways? *Proteomes* 2, 224-242.
- Barcelo A.R. (2005). Xylem parenchyma cells deliver the H₂O₂ necessary for lignification in differentiating xylem vessels. *Planta* 220, 747-756.

Belmonte M.F., Kirkbride R.C., Stone S.L., Pelletier J.M., Bui A.Q., Yeung E.C., Hashimoto M., Fei J., Harada M., Munoz M.D. et al. (2013). Comprehensive developmental profiles of gene activity in regions and subregions of the *Arabidopsis* seed. *Proceedings of the National Academy of Sciences of the United States of America* 110, E435-E444.

Braccini I., Grasso R.P., and Perez S. (1999). Conformational and configurational features of acidic polysaccharides and their interactions with calcium ions: a molecular modeling investigation. *Carbohydrate Research* 317, 119-130.

Bradford M.M. (1976). Rapid and sensitive method for quantification of microgram quantities of protein utilizing principle of protein-dye binding. *Analytical Biochemistry* 72, 248-254.

Burlat V., Ambert K., Ruel K., and Joseleau J.P. (1997). Relationship between the nature of lignin and the morphology of degradation performed by white-rot fungi. *Plant Physiology and Biochemistry* 35, 645-654.

Busse-Wicher M., Grantham N.J., Lyczakowski J.J., Nikolovski N., and Dupree P. (2016). Xylan decoration patterns and the plant secondary cell wall molecular architecture. *Biochemical Society Transactions* 44, 74-78.

Camborde L., Jauneau A., Briere C., Deslandes L., Dumas B., and Gaulin E. (2017). Detection of nucleic acid-protein interactions in plant leaves using fluorescence lifetime imaging microscopy. *Nature Protocols* 12, 1933-1950.

Carpin S., Crevecoeur M., de Meyer M., Simon P., Greppin H., and Penel C. (2001). Identification of a Ca(2+)-pectate binding site on an apoplastic peroxidase. *Plant Cell* 13, 511-520.

Carpita N.C., and Gibeaut D.M. (1993). Structural models of primary cell walls in flowering plants: Consistency of molecular structure with the physical properties of the walls during growth. *Plant Journal* 3, 1-30.

Clausen M.H., Willats W.G.T., and Knox J.P. (2003). Synthetic methyl hexagalacturonate hapten inhibitors of antihomogalacturonan monoclonal antibodies LM7, JIM5 and JIM7. *Carbohydrate Research* 338, 1797-1800.

Clough S.J., and Bent A.F. (1998). Floral dip: a simplified method for *Agrobacterium*-mediated transformation of *Arabidopsis thaliana*. *Plant Journal* 16, 735-743.

Driouich A., Follet-Gueye M.L., Bernard S., Kousar S., Chevalier L., Vire-Gibouin M., and Lerouxel O. (2012). Golgi-mediated synthesis and secretion of matrix polysaccharides of the primary cell wall of higher plants. *Frontiers in Plant Science* 3, 79.

Dumville J.C., and Fry S.C. (2000). Uronic acid-containing oligosaccharins: Their biosynthesis, degradation and signalling roles in non-diseased plant tissues. *Plant Physiology and Biochemistry* 38, 125-140.

Francoz E., Ranocha P., Burlat V., and Dunand C. (2015a). *Arabidopsis* seed mucilage secretory cells: regulation and dynamics. *Trends in Plant Science* 20, 515-524.

Francoz E., Ranocha P., Nguyen-Kim H., Jamet E., Burlat V., and Dunand C. (2015b). Roles of cell wall peroxidases in plant development. *Phytochemistry* 112, 15-21.

Francoz E., Ranocha P., Pernot C., Le Ru A., Pacquit V., Dunand C., and Burlat V. (2016). Complementarity of medium-throughput in situ RNA hybridization and tissue-specific transcriptomics: case study of *Arabidopsis* seed development kinetics. *Scientific Reports* 6, 24644.

Fry S.C. (1998). Oxidative scission of plant cell wall polysaccharides by ascorbate-induced hydroxyl radicals. *Biochemical Journal* 332, 507-515.

Fulton L.M., and Cobbett C.S. (2003). Two alpha-L-arabinofuranosidase genes in *Arabidopsis thaliana* are differentially expressed during vegetative growth and flower development. *Journal of Experimental Botany* 54, 2467-2477.

Gadjev I., Vanderauwera S., Gechev T.S., Laloi C., Minkov I.N., Shulaev V., Apel K., Inze D., Mittler R., and Van Breusegem F. (2006). Transcriptomic footprints disclose specificity of reactive oxygen species signaling in Arabidopsis. *Plant Physiology* 141, 436-445.

Guex N., and Peitsch M.C. (1997). SWISS-MODEL and the Swiss-PdbViewer: An environment for comparative protein modeling. *Electrophoresis* 18, 2714-2723.

Hall H.C., Cheung J., and Ellis B.E. (2013). Immunoprofiling reveals unique cell-specific patterns of wall epitopes in the expanding Arabidopsis stem. *Plant Journal* 74, 134-147.

Inoué S. (2006). Foundations of confocal scanned imaging in light microscopy. In *Handbook of biological confocal microscopy*, Pawley, J.B., ed. (New York: Springer Science+Business Media, LCC), pp. 1-19.

Irshad M., Canut H., Borderies G., Pont-Lezica R., and Jamet E. (2008). A new picture of cell wall protein dynamics in elongating cells of *Arabidopsis thaliana*: Confirmed actors and newcomers. *BMC Plant Biology* 8, 94.

Jolie R.P., Duvetter T., Van Loey A.M., and Hendrickx M.E. (2010). Pectin methylesterase and its proteinaceous inhibitor: a review. *Carbohydrate Research* 345, 2583-2595.

Kato N., Pontier D., and Lam E. (2002). Spectral profiling for the simultaneous observation of four distinct fluorescent proteins and detection of protein-protein interaction via fluorescence resonance energy transfer in tobacco leaf nuclei. *Plant Physiology* 129, 931-942.

Kelley L.A., Mezulis S., Yates C.M., Wass M.N., and Sternberg M.J.E. (2015). The Phyre2 web portal for protein modeling, prediction and analysis. *Nature Protocols* 10, 845-858.

Koncz C., and Schell J. (1986). The promoter of TL-DNA GENE 5 controls the tissue-specific expression of chimeric genes carried by a novel type of *Agrobacterium* binary vector. *Molecular & General Genetics* 204, 383-396.

Konig P., Krasteva G., Tag C., Konig I.R., Arens C., and Kummer W. (2006). FRET-CLSM and double-labeling indirect immunofluorescence to detect close association of proteins in tissue sections. *Laboratory Investigation* 86, 853-864.

Kunieda T., Shimada T., Kondo M., Nishimura M., Nishitani K., and Hara-Nishimura I. (2013). Spatiotemporal secretion of PEROXIDASE36 is required for seed coat mucilage extrusion in Arabidopsis. *Plant Cell* 25, 1355-1367.

Lee K.J.D., Dekkers B.J.W., Steinbrecher T., Walsh C.T., Bacic A., Bentsink L., Leubner-Metzger G., and Knox J.P. (2012). Distinct cell wall architectures in seed endosperms in representatives of the Brassicaceae and Solanaceae. *Plant Physiology* 160, 1551-1566.

Lee K.J.D., Marcus S.E., and Knox J.P. (2011). Cell wall biology: Perspectives from cell wall imaging. *Molecular Plant* 4, 212-219.

Lee Y., Rubio M.C., Alassimone J., and Geldner N. (2013). A mechanism for localized lignin deposition in the endodermis. *Cell* 153, 402-412.

Lee Y., Yoon T.H., Lee J., Jeon S.Y., Lee J.H., Lee M.K., Chen H.Z., Yun J., Oh S.Y., Wen X.H. et al. (2018). A lignin molecular brace controls precision processing of cell walls critical for surface integrity in Arabidopsis. *Cell* 173, 1468-+.

Levesque-Tremblay G., Muller K., Mansfield S.D., and Haughn G.W. (2015a). HIGHLY METHYL ESTERIFIED SEEDS is a Pectin Methyl Esterase involved in embryo development. *Plant Physiology* 167, 725-737.

Levesque-Tremblay G., Pelloux J., Braybrook S.A., and Muller K. (2015b). Tuning of pectin methylesterification: consequences for cell wall biomechanics and development. *Planta* 242, 791-811.

Mathé C., Barre A., Jourda C., and Dunand C. (2010). Evolution and expression of class III peroxidases. *Archives of Biochemistry and Biophysics* 500, 58-65.

Matsui T., Nakayama H., Yoshida K., and Shinmyo A. (2003). Vesicular transport route of horseradish C1a peroxidase is regulated by N- and C-terminal propeptides in tobacco cells. *Applied Microbiology and Biotechnology* 62, 517-522.

McFarlane H.E., Gendre D., and Western T.L. (2014). Seed coat ruthenium red staining assay. *Bio-protocol* 4, 1-4.

Mechin V., Baumberger S., Pollet B., and Lapierre C. (2007). Peroxidase activity can dictate the *in vitro* lignin dehydrogenative polymer structure. *Phytochemistry* 68, 571-579.

Morris G.M., Huey R., Lindstrom W., Sanner M.F., Belew R.K., Goodsell D.S., and Olson A.J. (2009). AutoDock4 and AutoDockTools4: Automated docking with selective receptor flexibility. *Journal of Computational Chemistry* 30, 2785-2791.

Morvan O., Quentin M., Jauneau A., Mareck A., and Morvan C. (1998). Immunogold localization of pectin methylesterases in the cortical tissues of flax hypocotyl. *Protoplasma* 202, 175-184.

Mouille G., Ralet M.C., Cavelier C., Eland C., Effroy D., Hematy K., McCartney L., Truong H.N., Gaudon V., Thibault J.F. et al. (2007). Homogalacturonan synthesis in *Arabidopsis thaliana* requires a Golgi-localized protein with a putative methyltransferase domain. *Plant Journal* 50, 605-614.

Nguyen-Kim H., Clemente H.S., Balliau T., Zivy M., Dunand C., Albenne C., and Jamet E. (2016). *Arabidopsis thaliana* root cell wall proteomics: Increasing the proteome coverage using a combinatorial peptide ligand library and description of unexpected Hyp in peroxidase amino acid sequences. *Proteomics* 16, 491-503.

North H.M., Berger A., Saez-Aguayo S., and Ralet M.C. (2014). Understanding polysaccharide production and properties using seed coat mutants: future perspectives for the exploitation of natural variants. *Annals of Botany* 114, 1251-1263.

Ostergaard L., Teilum K., Mirza O., Mattsson O., Petersen M., Welinder K.G., Mundy J., Gajhede M., and Henriksen A. (2000). Arabidopsis ATP A2 peroxidase. Expression and high-resolution structure of a plant peroxidase with implications for lignification. *Plant Molecular Biology* 44, 231-243.

Oudin A., Mahroug S., Courdavault V., Hervouet N., Zelwer C., Rodriguez-Concepcion M., St-Pierre B., and Burlat V. (2007). Spatial distribution and hormonal regulation of gene products from methyl erythritol phosphate and monoterpene-secoiridoid pathways in *Catharanthus roseus*. *Plant Molecular Biology* 65, 13-30.

Passardi F., Tognolli M., De Meyer M., Penel C., and Dunand C. (2006). Two cell wall associated peroxidases from Arabidopsis influence root elongation. *Planta* 223, 965-974.

Peaucelle A., Wightman R., and Hofte H. (2015). The control of growth symmetry breaking in the Arabidopsis hypocotyl. *Current Biology* 25, 1746-1752.

Pedersen H.L., Fangel J.U., McCleary B., Ruzanski C., Rydahl M.G., Ralet M.C., Farkas V., von Schantz L., Marcus S.E., Andersen M.C.F. et al. (2012). Versatile high resolution oligosaccharide microarrays for plant glycobiology and cell wall research. *Journal of Biological Chemistry* 287.

Perez S., Sarkar A., Rivet A., Breton C., and Imberty A. (2015). Glyco3D: a portal for structural glycosciences. *Methods in molecular biology (Clifton, N.J.)* 1273, 241-58.

Popper Z.A., Michel G., Herve C., Domozych D.S., Willats W.G.T., Tuohy M.G., Kloareg B., and Stengel D.B. (2011). Evolution and diversity of plant cell walls: From algae to flowering plants. *Annual Review of Plant Biology* 62, 567-588.

Ranocha P., Francoz E., Burlat V., and Dunand C. (2014). Expression of PRX36, PME16 and SBT1.7 is controlled by complex transcription factor regulatory networks for proper seed coat mucilage extrusion. *Plant signaling & behavior* 9, e977734.

Roppolo D., Boeckmann B., Pfister A., Boutet E., Rubio M.C., Denervaud-Tendon V., Vermeer J.E.M., Gheyselinck J., Xenarios I., and Geldner N. (2014). Functional and Evolutionary Analysis of the CASPARIAN STRIP MEMBRANE DOMAIN PROTEIN Family. *Plant Physiology* 165, 1709-1722.

Roppolo D., De Rybel B., Tendon V.D., Pfister A., Alassimone J., Vermeer J.E.M., Yamazaki M., Stierhof Y.D., Beeckman T., and Geldner N. (2011). A novel protein family mediates Casparian strip formation in the endodermis. *Nature* 473, 380-U564.

Saez-Aguayo S., Ralet M.C., Berger A., Botran L., Ropartz D., Marion-Poll A., and North H.M. (2013). PECTIN METHYLESTERASE INHIBITOR6 promotes Arabidopsis mucilage release by limiting methylesterification of homogalacturonan in seed coat epidermal cells. *Plant Cell* 25, 308-323.

Sainsbury F., Thuenemann E.C., and Lomonossoff G.P. (2009). pEAQ: versatile expression vectors for easy and quick transient expression of heterologous proteins in plants. *Plant Biotechnology Journal* 7, 682-693.

Scheler C., Weitbrecht K., Pearce S.P., Hampstead A., Buttner-Mainik A., Lee K.J.D., Voegelé A., Oracz K., Dekkers B.J.W., Wang X.F. et al. (2015). Promotion of testa rupture during Garden cress germination involves seed compartment-specific expression and activity of Pectin methylesterases. *Plant Physiology* 167, 200-215.

Schopfer P. (1996). Hydrogen peroxide-mediated cell-wall stiffening in vitro in maize coleoptiles. *Planta* 199, 43-49.

Schweikert C., Liskay A., and Schopfer P. (2000). Scission of polysaccharides by peroxidase-generated hydroxyl radicals. *Phytochemistry* 53, 565-570.

Seifert G.J., and Blaukopf C. (2010). Irritable walls: The plant extracellular matrix and signaling. *Plant Physiology* 153, 467-478.

Seki M., Carninci P., Nishiyama Y., Hayashizaki Y., and Shinozaki K. (1998). High-efficiency cloning of Arabidopsis full-length cDNA by biotinylated CAP trapper. *Plant Journal* 15, 707-720.

Seki M., Narusaka M., Kamiya A., Ishida J., Satou M., Sakurai T., Nakajima M., Enju A., Akiyama K., Oono Y. et al. (2002). Functional annotation of a full-length Arabidopsis cDNA collection. *Science* 296, 141-145.

Sénéchal F., L'Enfant M., Domon J.M., Rosiau E., Crepeau M.J., Surcouf O., Esquivel-Rodriguez J., Marcelo P., Mareck A., Guérineau F. et al. (2015). Tuning of Pectin Methylesterification PECTIN METHYLESTERASE INHIBITOR 7 modulates the processive activity of co-expressed PECTIN METHYLESTERASE 3 in a pH-dependent manner. *Journal of Biological Chemistry* 290, 23320-23335.

Shah K., Penel C., Gagnon J., and Dunand C. (2004). Purification and identification of a Ca²⁺-pectate binding peroxidase from Arabidopsis leaves. *Phytochemistry* 65, 307-312.

Shi D.C., Ren A.Y., Tang X.F., Qi G., Xu Z.C., Chai G.H., Hu R.B., Zhou G.K., and Kong Y.Z. (2018). MYB52 negatively regulates pectin demethylesterification in seed coat mucilage. *Plant Physiology* 176, 2737-2749.

Singh B., Avci U., Inwood S.E.E., Grimson M.J., Landgraf J., Mohnen D., Sorensen I., Wilkerson C.G., Willats W.G.T., and Haigler C.H. (2009). A specialized outer layer of the primary cell wall joins elongating cotton fibers into tissue-like bundles. *Plant Physiology* 150, 684-699.

Sujatha M.S., Sasidhar Y.U., and Balaji P.V. (2004). Energetics of galactose- and glucose-aromatic amino acid interactions: Implications for binding in galactose-specific proteins. *Protein Science* 13, 2502-2514.

Trott O., and Olson A.J. (2010). Software news and update AutoDock Vina: Improving the speed and accuracy of docking with a new scoring function, efficient optimization, and multithreading. *Journal of Computational Chemistry* 31, 455-461.

Tsai A.Y.L., Kunieda T., Rogalski J., Foster L.J., Ellis B.E., and Haughn G.W. (2017). Identification and characterization of Arabidopsis seed coat mucilage proteins. *Plant Physiology* 173, 1059-1074.

Turbant A., Fournet F., Lequart M., Zabijak L., Pageau K., Bouton S., and Van Wuytswinkel O. (2016). PME58 plays a role in pectin distribution during seed coat mucilage extrusion through homogalacturonan modification. *Journal of Experimental Botany* 67, 2177-2190.

Verhertbruggen Y., Marcus S.E., Haeger A., Ordaz-Ortiz J.J., and Knox J.P. (2009). An extended set of monoclonal antibodies to pectic homogalacturonan. *Carbohydrate Research* 344, 1858-1862.

Warinowski T., Koutaniemi S., Karkonen A., Sundberg I., Toikka M., Simola L.K., Kilpelainen I., and Teeri T.H. (2016). Peroxidases bound to the growing lignin polymer produce natural like extracellular lignin in a cell culture of Norway Spruce. *Frontiers in Plant Science* 7, 1523.

Weber E., Gruetzner R., Werner S., Engler C., and Marillonnet S. (2011). Assembly of designer TAL effectors by Golden Gate cloning. *Plos One* 6, e19722.

Western T.L. (2012). The sticky tale of seed coat mucilages: production, genetics, and role in seed germination and dispersal. *Seed Science Research* 22, 1-25.

Wi S.G., Singh A.P., Lee K.H., and Kim Y.S. (2005). The pattern of distribution of pectin, peroxidase and lignin in the middle lamella of secondary xylem fibres in alfalfa (*Medicago sativa*). *Annals of Botany* 95, 863-868.

Willats W.G.T., Orfila C., Limberg G., Buchholt H.C., van Alebeek G., Voragen A.G.J., Marcus S.E., Christensen T., Mikkelsen J.D., Murray B.S. et al. (2001). Modulation of the degree and pattern of methyl-esterification of pectic homogalacturonan in plant cell walls - Implications for pectin methyl esterase action, matrix properties, and cell adhesion. *Journal of Biological Chemistry* 276, 19404-19413.

Wolf S., Mouille G., and Pelloux J. (2009). Homogalacturonan methyl-esterification and plant development. *Molecular Plant* 2, 851-860.

FIGURE LEGEND

Figure 1. *PRX36* and *PMEI6* are co-expressed during seed development whereas *prx36-1* and *pmei6-1* mutants display a similar seed mucilage release defect phenotype.

A: Similar tissue-specific expression profile for *PRX36* and *PMEI6* as displayed on the seed data source of eFP browser (see STAR Methods). **B:** *PMEI6* is the first hit of the *PRX36* co-expression network using the tissue-specific seed developmental kinetics GSE12404 dataset (Belmonte et al., 2013). **C-H:** Ruthenium red seed mucilage release tests show a similar mucilage release defect phenotype for *prx36-1* and *pmei6-1* as compared to Col-0. **I-N:** Nomarski observation of imbibed seeds shows similar abnormal peeling of intact portions of the outer wall from MSCs (*) in *prx36-1* and *pmei6-1*. RK, rank; PCC, Pearson Correlation Coefficient; EP, embryo proper; SUS, suspensor; MCE, micropylar endosperm; PEN, peripheral endosperm; CZEN, chalazal endosperm; CZSC, chalazal seed coat; SC, seed coat; WS, whole seed; RR, Ruthenium red; Bars: 100 μ m. See also Figure S1.

Figure 2. The outer cell wall domain localization of PRX36-GFP in developing seed MSCs is impaired following treatment with pectin-modifying solutions.

ca. 7 DAP developing seeds of plants expressing *proPRX36:PRX36-GFPg4* (Kunieda et al., 2013) were imaged by confocal microscopy during time course of chemical treatment using

either sodium phosphate (NaP) buffer (**A**, **B**, control), Na₂CO₃ (**C**, **D**, demethylesterification agent) or EDTA (**E**, **F**, calcium chelation agent). Time of post-treatment imaging: Ti, 5 min (**A**), 10 min (**C**), 8 min (**E**); Tf, 155 min (**B**), 180 min (**D**), 120 min (**F**). Column 1: Whole seed maximum projection view of Z stacks. Column 2: Confocal section of the white inset in column 1. Column 3: orthogonal view along the red axis displayed in column 2. Column 4: transmitted light view of the images shown in column 2. Column 5: semi quantitative analysis of trans-cellular fluorescence profiles (one example is shown with a yellow line in the images of column 2), n > 20 cells. arrow, position of the outer cell wall domain; m, mucilage; a, amyloplasts. Bars: 50 μm (column 1); 25 μm (columns 2-4).

Figure 3. AtPRX36-TagRFP is stably localized to the outer cell wall domain during seed MSC development in Col-0 and *prx36-1*, but is mislocalized in *pmei6-1* and *prx36-1* × *pmei6-1*.

A: The *proPRX36:PRX36-TagRFP* construct was expressed in the four genetic backgrounds labeled on the left. The time course of fluorescence observed in MSCs by spinning disk confocal microscopy is displayed for one representative line for each construct. Laser power intensity of 7% for all images. The plots on the right show the semi-quantitative analysis of the MSC fluorescence profile taken at 12 DAP for 5 cells from 3 independent transformed lines (black, red, blue lines, respectively) for each genetic background. **B:** Example of semi-quantitative analysis of the fluorescence profile along a transversal axis of one MSC in two contrasted examples. Bars: 200 μm.

Figure 4. The PRX36 immunofluorescence labeling to the outer cell wall domain of seed MSCs necessitates the co-localization of PME16-dependent partially methylesterified homogalacturonan LM20 epitopes.

A: Whole-microscopy slide views of Nanozoomer scans of sections of paraffin-embedded tissue microarrays of developing siliques from Col-0, *prx36-1* and *pmei6-1* enable studying hundred of seeds at various developmental stages. **B:** Double immunofluorescence labeling with αPRX36/A488 and LM20/A555 as indicated on the left. Extraction views from 40× scans were assembled to display the two individual fluorescence channels as well as the merge of these channels and the bright-field (BF) views for the three genotypes at 6 developmental stages. No individual treatment of images was performed to enable comparison between patterns/intensities. These images are representative of numerous observations (n > 50 MSCs). Bars: 2.5 mm (A); 25 μm (B). See also Figures S2, S3.

Figure 5. FRET- FLIM immunofluorescence shows that co-localized αPRX36 and JIM7 or LM20 immunocomplexes are in 10 nm vicinity.

A: Example of images obtained following whole slide scanning of double immunofluorescence labeling performed on mature green developing seeds (12 DAP) with α PRX36/A488 *vs* LM20/A555 (**red frame**) or *vs* JIM7/A555 (**orange frame**) or *vs* LM25/A555 (**blue frame**). Control simple labeling: α PRX36/A488 (**green frame**). The acquisition modes (Filtersets or bright-field (BF)) and merge are indicated on the left. Examples of regions of interest (ROIs) used for FRET-FLIM analysis are also displayed. Bars: 20 μ m. **B:** Histogram showing the distribution of the lifetime of the Alexa488 FRET donor (τ_{A488}) in absence (green) or presence (red, orange, blue) of potential FRET receiver in 30 ROIs each (same color code as in A). The mean τ and SEM are displayed in color-coded frame. The occurrence of FRET is evaluated by calculating the $\Delta\tau$ (donor A488 lifetime without A555 acceptor - donor A488 lifetime with A555 acceptor) and the corresponding *p*-values (Student's T-test). When statistically significant (*p*-value < 0.001), $\Delta\tau$ is used to calculate the FRET % and the Förster distance (*d*) between the immunocomplexes (see text and STAR methods for details). See also Figure S4.

Figure 6. The *in silico* predicted hexagalacturonate-PRX36 docking valley is necessary both for *in vivo* stable localization of PRX36-TagRFP to the outer cell wall domain and for functional complementation of the mucilage release phenotype.

A: Hexagalacturonate n^o3 (oo888o) with o = non methylated galacturonic acid and 8 = methylesterified galacturonic acid displaying the best recognition by JIM7 (Clausen et al., 2003) and the best docking prediction on PRX36 (Figure S5) was used to build *in silico* docking models with PRX36, PRX50 and PRX36m. Red and blue color code inside the predicted binding valley corresponds to polar positive and hydrophobic amino acids, respectively; yellow and green color code within the valley corresponds to missing polar positive and missing hydrophobic amino acids, respectively (See Figure S6 for details). **B:** Genotypes used including Col-0, *prx36-1*, and for each of the three proteins, 3 independent *prx36-1* genetic lines transformed with *promPRX36:PRX-TagRFP* constructs. **C-F:** Experimental validation that *in silico* selected PRX36-specific amino acids are necessary for correct localization of the TagRFP fusion protein to the outer cell wall domain (**C**) and for the correct mucilage release (**D-E**). **C:** Confocal spinning disk microscopy *in vivo* observation of TagRFP fluorescence in MSCs of developing seeds at 7, 9, 10 and 12 DAP. The white numbers in top right corner of individual images indicate the laser power intensity used. **D-F:** Mucilage release test phenotype following ruthenium red staining (**D**) and quantification and

statistical analysis of the results using the mucilage area (**E**) and mucilage circularity (**F**) as parameters. Mean values \pm SEM (two independent repeats, total n = 199-326 seeds) are represented with a yellow-to-red heatmap. The *p*-values correspond to the Student's T-test statistical analysis of the results as compared to Col-0. Bars: 20 μ m (**C**); 200 μ m (**D**). See also Figures S5, S6, S7.

Figure 7. Ultrastructural phenotyping of the dry seed MSC cell wall domain and spatio-temporal integrated model. **A:** Transmission electron microscopy observation of Col-0, *prx36-1* and *pmei6-1* dry seed MSCs shows the outer wall domain thinning in Col-0 and thickening in *prx36-1* and *pmei6-1*. Unprocessed images and false colored images are presented. Primary wall: blue; columella secondary wall: green, mucilage: pink; arrows, outer wall domain. Scale bars: 5 μ m (wide view); 0.5 μ m (zooms). **B:** simplified model showing the molecular relationship between PME16 and PRX36. 8: methylesterified galacturonic acid; o: demethylated galacturonic acid. **C:** Integrated model showing the cell wall dynamics of MSCs and the *PME16/PRX36* gene expression (open bars), PRX36 accumulation in the outer wall domain (grey bar) and hypothesized PRX36 activity (black bar). DAP: days after pollination.

STAR METHODS

CONTACT FOR REAGENT AND RESOURCE SHARING

Further information and requests for resources and reagents should be directed to and will be fulfilled by the Lead Contact, Vincent Burlat (burlat@lrsv.ups-tlse.fr).

EXPERIMENTAL MODEL AND SUBJECT DETAILS

Plant material and growth conditions

A. thaliana wild-type Col-0 (accession number N1093) and *prx36-1* T-DNA insertion mutant (SAIL_194_G03) (Kunieda et al., 2013) were obtained from the European Arabidopsis Stock Centre (<http://arabidopsis.info/>). *pmei6-1* mutant (SM_3.19557) (Saez-Aguayo et al., 2013) and *proPRX36:PRX36-GFPg4/prx36-1* (*proPER36:PER36-GFPg4/per36-1*) (Kunieda et al., 2013) seeds were given by Dr Helen North (IJPB, Versailles, France) and Dr Ikuko Hara-Nishimura (Kyoto University, Japan), respectively. *pmei6-1* was crossed with *prx36-1*. The mutations (*pmei6-1*, *prx36-1*) were characterized by PCR-based methods (Key Resources Table).

Plants were routinely grown in Jiffy peat pellets (continuous light, 120 $\mu\text{mol photons/m/s}$, 22°C, 67% relative humidity). For *in vitro* experiments, seeds were surface-sterilized and sown in Petri dishes on agar-solidified MS medium including sucrose (10 g.L^{-1}), and grown in a culture room with continuous light (120 $\mu\text{mol photons.m}^{-1}.\text{s}^{-1}$, 22°C).

Nicotiana benthamiana plants were cultivated in growth chambers (16 h light/8 h dark cycle, 25/22°C, 80% humidity) during 4 weeks.

METHOD DETAILS

Transcriptomic data mining

PRX36 and *PMEI6* seed-specific expression profiles were obtained using the seed data source of eFP browser (<http://bar.utoronto.ca/efp/cgi-bin/efpWeb.cgi?dataSource=Seed>). Tissue-specific seed development transcriptomic data (Belmonte et al., 2013) was analyzed as described (Francoz et al., 2016; Francoz et al., 2015a) in order to build the *PRX36* co-expression network. A red (max value)-to yellow (minimum value)-to grey (value below the 45 cutoff value) relative heatmap was drawn using Microsoft Excel.

Ruthenium red mucilage release test, image analysis and statistical analysis

For high-throughput mucilage release semi-quantitative phenotyping, a protocol adapted from (McFarlane et al., 2014) was used. About 100-200 seeds were vigorously shaken (250 rpm) for 1 h in 1.4 mL 0.01M Tris-HCl pH7.5 in a microtube in horizontal position. After gentle spinning for a few seconds, the solution was carefully removed. Seeds were sequentially rinsed with 1 mL 0.01M Tris-HCl pH7.5, stained in 1.4 mL 0.02 % (w/v) ruthenium red in 0.01M Tris-HCl pH7.5 for 1 h at 250 rpm, washed twice with 1 mL 0.01M Tris-HCl pH7.5 and carefully transferred in a 24-well microplate. The plate was scanned at 6400 dpi in transparent mode using an Epson perfection V100 photo scanner. Images were analyzed with ImageJ (<https://imagej.nih.gov/ij/>) using a .txt macro command in order to measure various phenotypical parameters at high-throughput:

```
title=getTitle();
run("Properties...", "channels=1 slices=1 frames=1 unit= $\mu\text{m}$  pixel_width=4.1344 pixel_height=4.1344 voxel_depth=4.1344 global");
run("Subtract Background...", "rolling=100 light separate sliding");
run("Split Channels");
selectWindow(title+" (blue)");
close();
//threshold the seed (without mucilage) and add the selection to the ROI manager.
selectWindow(title+" (red)");
run("Threshold...");
waitForUser("All the seeds", "highlight in red the center part of all the seeds (black shape)");
setOption("BlackBackground", false);
run("Create Selection");
roiManager("Add");
```

```

roiManager("Select", 0);
roiManager("Rename", "All seeds ");
//threshold seeds and theirs mucilage
selectWindow(title+" (green)");
run("Threshold...");
waitForUser("complete seed", "highlight in red the seeds and their mucilage ");
setOption("BlackBackground", false);
run("Convert to Mask");
run("Watershed");
run("Set Measurements...", "area centroid perimeter shape feret's display redirect=None decimal=3");
run("Analyze Particles...", "size=200000-Infinity show=Masks exclude summarize add");
Dialog.create("Count");
Dialog.addNumber("Please indicate the value define in the count field in the summary window ",1);
Dialog.show();
n=Dialog.getNumber();
for(i=1;i<=n;i++)
{
roiManager("Select", i);
roiManager("Rename","complete seed"+ i);
}
for(i=1;i<=n;i++)
{
roiManager("Select", newArray(0,i));
roiManager("AND");
roiManager("Add");
roiManager("Select", n+i);
roiManager("Rename", "seed "+i);
}
roiManager("Show All");
roiManager("Measure");

```

The mucilage area (μm^2) and the mucilage circularity (0-1 range) were retained as representative parameters for phenotyping. Data was analyzed using Microsoft Excel and statistical Student's t tests were run using the R package (<https://www.r-project.org/>). The figure was assembled using Corel Photo-Paint, reproducing the RGB colors of the color-coded heat maps generated with Microsoft Excel.

RNA isolation and transcript analysis by RT-PCR

New flowers with emerging petals were marked daily with color-coded strings and, at 5 to 14 days after pollination (DAP), total RNA was prepared from 6 siliques of each developmental stage/genotype with the Tri-reagent solution (Sigma-Aldrich, St Louis, MO, USA) according to the manufacturer's instructions. After quantification by spectrophotometry and confirmation by electrophoresis, 1 μg of the crude RNA preparation was treated with one unit of RQ1 RNase-free DNase I (Promega, Madison, WI, USA). First-strand cDNA was synthesized using the M-MLV system (Promega) and PCR was performed with gene-specific intron-spanning primers (Key Resources Table). The amount of cDNA template in each RT-PCR was normalized to the signal from the actin-encoding *ACT2* gene (Fulton and Cobbett, 2003). Following electrophoresis and ethidium bromide staining, RT-PCR products were quantified. Three experiments were carried out with consistent results.

Protein extract and analysis by Western blotting

Eight developing siliques at 6 DAP and four siliques at 8, 10, 12 and 14 DAP from Col-0, *prx36-1* or *pmei6-1* were microdissected to remove the valves. The remaining replums containing seeds were gathered in 2 mL microtubes containing a metallic ball, weighed (4 to 8 mg per sample), frozen in liquid nitrogen and stored at -80°C. Samples were grinded 4 times 45 s at 30 Hz using a Retsch MM400 ball mill.

Cell wall protein-enriched fractions were obtained using 4 µL of extraction buffer/mg sample [1 mL of 5 mM sodium acetate buffer 0.2 M CaCl₂ pH 4.6 extemporaneously completed with 1 µL mercaptoethanol and 1.5 µL protease inhibitor cocktail (Sigma-Aldrich) adapted from (Irshad et al., 2008)]. Samples were further thoroughly agitated for 15 min at 4°C at 400 rpm and individually strongly vortexed. Four µL of denaturing solution/mg sample were mixed before analysis (Kato et al., 2002). Following SDS-PAGE and transfer, nitrocellulose membranes were successively stained with Ponceau Red, imaged, rinsed and saturated overnight with 5% non fat dry milk in TTBS (20 mM Tris-HCl pH 7.5, 500 mM NaCl, 0.05% Tween 20). αPRX36 antibody was incubated for 5 h at RT (1:1000 in TTBS-5% milk) and secondary goat anti-rabbit IgG-alkaline phosphatase conjugate (Sigma) was incubated for 2 h at RT (1:5000 in TTBS 5% milk). BCIP-NBT reaction was performed for 50 min.

Sequence analysis, homology modeling and binding simulation

Sequence and multiple alignment analysis was performed using BioEdit (<http://www.mbio.ncsu.edu/BioEdit/bioedit.html>) with final sequence edition using Corel Photo-Paint.

Homology model for PRX36 (UniProt accession number Q9SD46) was built with the Phyre2 server (Kelley et al., 2015). The PRX36 structural model used in this study was the Phyre2 prediction with the highest ranking score (Confidence: 100.0%; Coverage: 88%). The template was the crystallographic structure (X-Ray diffraction, 1.45 Å) of *A. thaliana* PRX53 (At5g06720; Protein Data Bank no. 1PA2) (Ostergaard et al., 2000).

α-D-(1-4) polygalacturonic acid structural model (Braccini et al., 1999) was retrieved from the Glyco3D portal (Perez et al., 2015)

(<http://glyco3d.cermav.cnrs.fr/mol.php?type=polysaccharide&molecule=2504>) and was modified to build the five hexagalacturonate models used to establish JIM7 specificity (Clausen et al., 2003).

AutoDock Tools (Morris et al., 2009) and AutoDock Vina (Trott and Olson, 2010) were used for simulating the binding of the partially methylesterified hexagalacturonates to PRX36,

PRX50 or PRX36m within a search box encompassing the whole target protein. Structural models were visualized and analyzed with Swiss-PdbViewer (Guex and Peitsch, 1997). The visualization of the models, color edition and identification of the amino acids distant of less than 5 Å from the best hexagalacturonate docking models were performed using Swiss-PdbViewer (Guex and Peitsch, 1997) (<http://www.expasy.org/spdbv/>).

TagRFP reporting constructs, plant transformation and selection

Primers used for vector construction are listed in Key Resources Table. *A. thaliana* *PRX36* (At3g50990) and *PRX50* (At4g37520) coding sequences were amplified by PCR from the RIKEN BioResource Center (<https://www.brc.riken.jp>) full-length cDNA clones RAFL22-03-B11 and RAFL06-08-C18, respectively (Seki et al., 2002; Seki et al., 1998). The *TagRFP* coding sequence was amplified from the TagRFP-AS-N vector (Evrogen). The *A. thaliana* *PRX36* promoter sequence (2635 bp) (Kunieda et al., 2013) and mutated *PRX36* (*PRX36m*) coding sequences were synthesized by GenScript (Piscataway, NJ, USA).

The different parts of the reporting constructs (*i.e.* *PRX36* promoter, CIII PRX coding sequences, *TagRFP* coding sequence) were assembled into the binary vector pL2V-Hyg, a gift from Dr Pierre-Marc Delaux (Plant Science Research Laboratory (LRSV), Auzeville, France) via Golden Gate cloning (Weber et al., 2011). Every construct was checked by restriction analysis and sequencing, and transferred into *Agrobacterium tumefaciens* GV3101::pMP90 strain (Koncz and Schell, 1986) for floral-dip transformation of *A. thaliana* (Clough and Bent, 1998). *proPRX36:PRX36-TagRFP* construct was transformed in Col-0, *prx36-1*, *pmei6-1* and *prx36-1* × *pmei6-1* plants. *proPRX36:PRX50-TagRFP* and *proPRX36:PRX36m-TagRFP* constructs were transformed in *prx36-1* plants. Seeds were selected on Murashige and Skoog (MS) medium containing hygromycin. Three independent homozygous transformed plant lines were studied for each construct.

PRX36-TagRFP and *PRX36m-TagRFP* coding sequences were amplified by PCR from their pL2V-Hyg counterparts (see above) with the primers listed in Key Resources Table. The PCR products were subcloned (LR reaction, Gateway Technology, Invitrogen) into pEAQ-HT-DEST1 vector to allow 35S prom-driven overexpression of the constructs *in planta* (Sainsbury et al., 2009). Every construct was checked by restriction analysis and sequencing, and transferred into *A. tumefaciens* GV3101::pMP90 strain. Transformed *A. tumefaciens* strains (OD 0.5 at 600 nm) were infiltrated into 30-day old *Nicotiana benthamiana* leaves. Forty-eight hours after infiltration leaves were detached, mounted in water and used for

confocal laser scanning microscopy. Transformed leaves were also harvested for CIII PRX activity measurement.

PRX36-TagRFP and PRX36m-TagRFP activity measurement

N. benthamiana leaves overexpressing PRX36-TagRFP, PRX36m-TagRFP were dissected and weighted (40-60 mg) and frozen in liquid nitrogen. Leaves transformed with the pEAQ empty vector were used as negative controls. Tissues were grinded twice 3 min at 30 Hz using a Retsch MM400 ball mill, with a quick spin between the two cycles. Soluble proteins were extracted in the following extraction buffer (50 μ l for 100 mg leaves): 20 mM HEPES, pH 7.0, 1 mM EGTA, 10 mM vitamin C, and PVP PolyclarAT (100 mg.g⁻¹ fresh weight). The extract was centrifuged twice 10 min at 10,000 \times g (4°C) to remove insoluble material. The protein content was determined using the Bradford reagent (Serva) with bovine serum albumin (Sigma-Aldrich) as a standard (Bradford, 1976). CIII PRX activity was measured at 25°C by following the oxidation of 8 mM guaiacol (Fluka) at 470 nm in the presence of 2 mM hydrogen peroxide (Carlo Erba) in a phosphate buffer (200 mM, pH 6.0). Results were expressed in nanokatals / mg proteins \pm SD (n \geq 4).

***In vivo* microscopy**

Confocal laser scanning microscopy:

Developing seeds of plants expressing *proPRX36*:PRX36-GFPg4 (Kunieda et al., 2013) were screened for GFP fluorescence and positive seeds (*circa* 7 DAP) were imaged with a SP2 AOBS confocal microscope (Leica) following time course series of three treatments. Seeds were mounted under a coverslip either in 0.1 M sodium phosphate buffer pH 7.5 (control), 0.1 M Na₂CO₃ pH 10.5 used as a demethylesterification agent (Singh et al., 2009) or 0.1 M EDTA pH 8.0 (calcium chelating agent). Observations were performed under a FLUO PLAN 40x/1.3 oil objective and GFP was excited by a 488nm laser and fluorescence was collected between 497 and 563 nm on PMT detector. The same settings were used for all the samples enabling comparison. Z stacks and orthogonal projections were performed using ImageJ. Transiently transformed *N. benthamiana* leaves were observed 48 h post agroinfiltration using an upright confocal laser scanning microscope (LEICA SP2 AOBS13) with a 40 x apochromatic water immersion lens. TagRFP fluorescence was imaged with the following settings (excitation: 561 nm; emission: 582–622 nm). Z stacks were performed using ImageJ.

Spinning disk confocal laser scanning microscopy:

Developing siliques taken at 5 to 12 DAP from plants expressing the different TagRFP constructs in various genetic backgrounds were dissected and the replums containing the seeds were mounted in distilled water. Given the high number of samples to observe (3 individual transformed lines \times 7 construct/genetic background \times 8 developing stages \times at least 2 repeats), we took advantage of the high throughput possibilities of spinning disk confocal microscopy. Images were taken with a PLAN APO 20x/0.75 dry objective using the confocal spinning disk microscope from Perkin Elmer driven by the Volocity 6.3.0 software and equipped with a Yokogawa CSU-X1 scan head, two EmCCD Hamamatsu C9100-13 cameras (Hamamatsu, Hamamatsu City, Japan) and a 580 nm beam splitter to separate dual staining on the 2 cameras. Images were sequentially acquired for TagRFP fluorescence then chloroplast autofluorescence used as control. TagRFP was excited with a 561 nm laser (Laser power intensity: 7% (Figure 3A) and 2% to 15% (Figure 6C), exposure time: 200 msec, gain: 5, sensitivity: 148) and the fluorescence was selected between 580 and 656 nm. Chloroplast autofluorescence was excited with a 561 nm laser and the fluorescence was detected with a 656 long-pass filter. Image analysis was performed with ImageJ building Z stacks in average intensity mode for Figure 3 and maximum intensity for Figure 6. The more subtle mislocalization observed in *pmei6-1* and *prx36-1 x pmei6-1* backgrounds was additionally analyzed with ImageJ plotting the superimposed relative fluorescence intensity profile of 5 MSCs for each individually transformed lines at 12 DAP.

***In situ* microscopy**

Developing seed paraffin embedding:

Developing siliques (5 to 14 DAP) were fixed in FAA and embedded in paraplast tissue microarrays (Francoz et al., 2016) reconstructing developmental kinetics of about 20 sorted siliques for Col-0, *prx36-1* and *pmei6-1* genetic backgrounds, respectively.

Dry seed resin embedding:

Dry seeds were embedded in LR White resin following an original optimized protocol to avoid breaking the outer cell wall and the release of the mucilage that would occur during classical aqueous fixation. In brief, dry seeds were individually punctured with a 60 μ m needle under a dissecting microscope and immersed in 1.25% glutaraldehyde/2% paraformaldehyde in 0.05 M PIPES, 5 mM EGTA, 5 mM MgSO₄, pH 6.9 buffer (Lee et al., 2012) complemented with 0.1% Triton X-100 and 50% ethanol. Five 1-min vacuum cycles allowed the fixative infiltration and the samples were fixed for 2 h at RT. Dry seeds were

washed in 50% ethanol and rapidly pre-embedded in a 2% low-melting agarose in a 0.5mL microtube used as a mold. At this step, the agarose allowed either to gather 5-7 seeds or to keep individual seeds, for later semi- and ultra-thin sectioning, respectively. Agarose-embedded seed samples were further dehydrated in an ethanol series up to 70%. After an overnight incubation in 70% ethanol, agarose-embedded samples were transferred in samples holders dedicated to automatic microwave tissue processor for electron microscopy (Leica EM AMW) using the following infiltration program:

70% ethanol (1 min, 37°C), 75% acetone (1 min, 37°C), 95% acetone (1 min, 37°C), LRW/95% acetone (1:3; v:v, 6 min, 37°C), LRW/95% acetone (1:1; v:v, 6 min, 40°C), LRW/95% acetone (3:1; v:v, 6 min, 45°C), LRW (6 min, 50°C, twice).

The samples are finally transferred to gelatin capsule and polymerized 24 h at 50°C.

Antibodies and CBM:

The α PRX36 specific antibody was raised in New Zealand rabbits against the selected PRX36 immunogenic peptide (C)SLIGSMENIPSPES conjugated to Keyhole limpet hemocyanin (KLH) used as an hapten (<https://www.genscript.com/>). Care was taken to select an immunogenic peptide distant from the putative PRX36 HG-binding valley. The affinity purified antibodies against the immunogenic peptide presented an ELISA titer of 1:128,000. The specificity of this antibody was further demonstrated by western immunoblot, immunofluorescence and immunogold labeling on Col-0 vs *prx36-1* samples. An attempt to produce a similar antibody for PME16 was performed using (C)RTLNADEFQRQISD PME16 immunogenic peptide but resulted in a useless unspecific antibody. Rat monoclonal JIM7, JIM5, LM18, LM19, LM20 (recognizing various methylesterification patterns of HGs), LM6, LM25 and LM21 (specific to other cell wall polysaccharides) were obtained at PlantProbes (<http://www.plantprobes.net/index.php>). The three monoclonal antibodies that appeared to be relevant for this study are JIM7 specific for partially methylesterified hexagalacturonans as defined by competitive inhibition ELISAs (Clausen et al., 2003), LM20 providing similar labeling as JIM7 despite no extensive characterization (Verhertbruggen et al., 2009) and LM25 specific to fucosylated and non-fucosylated xyloglucans (Pedersen et al., 2012). CBM3a-His Tag, a carbohydrate-binding module (CBM) His-tag recombinant protein from *Clostridium thermocellum* directed to crystalline cellulose was purchased at PlantProbes.

Double immunofluorescence labeling and FRET-FLIM analysis:

Double immunofluorescence labeling experiments were performed on 12 μm -serial section from paraffin embedded developing siliques containing seeds with αPRX36 and LM20, JIM7 or LM25 primary antibodies (1:10 dilution each, 3 h incubation with both antibodies together) followed by anti-rabbit IgG-Alexa Fluor 488 (Invitrogen A11034) and anti-rat IgG-Alexa Fluor 555 (Invitrogen A21434) secondary antibodies (1:100 dilution each, 1h incubation with both antibodies together) following previously described protocol (Oudin et al., 2007). Simple labeling combinations of primary and secondary antibodies also performed as well as negative controls to validate the absence of cross reactivity of species-specific secondary antibodies. Similarly, sections were double labeled with αPRX36 and CBM3a, JIM7 and CBM3a, or LM25 and CBM3a (1:10 dilution for αPRX36 , JIM7 and LM25, 20 $\mu\text{g.mL}^{-1}$ for CBM3a) followed by anti-rabbit IgG-Alexa Fluor 488 to detect αPRX36 (Invitrogen A11034) or anti-rat IgG-Alexa Fluor 488 (Invitrogen A11006) to detect JIM7 or LM25, and anti-His Tag-Alexa Fluor 555 to detect CBM3a (Invitrogen MA1-135-A555) secondary antibodies (1:100 and 1:50 dilution respectively, 1h incubation with both antibodies together). Simple indirect labeling of αPRX36 -A488, JIM7-A488 or LM25-A488 was also performed to provide FRET-FLIM controls. Slides were mounted in Prolong Gold antifade (Molecular probes P36934) and scanned using a Nanosizer 2.0RS scanner (Hamamatsu) at 40 \times . The FITC (excitation: 482/18 nm; dichroic mirror 488 nm; emission: 525/30 nm) and TRITC (excitation: 563/9 nm; dichroic mirror 561 nm; emission: 607/36 nm) filter sets were used sequentially to visualize Alexa488 and Alexa555 fluorescence, respectively. The bright field (BF) mode was also sequentially used to visualize the morphology. Scans were analyzed using NDP view (Hamamatsu) and extracted images for the comparative time course of fluorescence pattern in Col-0, *prx36-1* and *pmei6-1*, as well as for the labeling specificity analysis were assembled in figures using Corel Photo-Paint.

The Rayleigh criterion allows calculating the theoretical xyz resolution of fluorescence signals in confocal microscopy (Inoué, 2006). We used: Alexa fluor 488 ($\lambda_{\text{em}} = 525 \text{ nm}$), a numerical aperture of the 63 \times objective ($\text{NA} = 1.4$), and immersion oil refractive index ($\eta = 1.518$). Applying these parameters to the theoretical formulae giving the xy resolution: ($\delta_{xy} = (0.61 \times \lambda_{\text{em}}) / (\sqrt{2} \times \text{NA})$) and the z resolution: ($\delta_z = (2 \times \lambda_{\text{em}} \times \eta) / (\sqrt{2} \times \text{NA}^2)$) for confocal fluorescence signals leads to $\delta_{xy} = 161 \text{ nm}$ and $\delta_z = 574 \text{ nm}$. This illustrates how colocalization of fluorescence signals in confocal scanning microscopy is far from demonstrating the molecular proximity of the fluorochromes. Therefore, αPRX36 -A488/LM20-A555, αPRX36 -A488/JIM7-A555, αPRX36 -A488/LM25-A555, αPRX36 -

A488/CBM3-A555, JIM7-A488/CBM3a-A555 and LM25-A488/CBM3a-A555 co-localized signals were additionally analyzed by fluorescence resonance energy transfer (FRET) approach coupled to fluorescence lifetime imaging microscopy (FLIM) using the technology recently described (Camborde et al., 2017) in order to evaluate the proximity of co-localized immunocomplexes at the nm scale. We focused the analysis on the Col-0 seeds at 12 DAP. The reference of Alexa Fluor 488 mean lifetime (τ A488) was determined using α PRX36-A488, JIM7-A488, or LM25-A488 simple indirect labeling experiments measuring 20-30 regions of interest (ROIs) for each control. The Alexa Fluor 488 mean lifetime in presence of the acceptor (τ A488.A555) was measured using the double labeling experiments previously described. The experiment was repeated thrice independently. In the case of a Gaussian distribution of the individual measured A488 lifetime values ($n=30$), the statistical significance of $\Delta\tau = \tau$ A488 – τ A488.A555 was assessed with a student's T test. When $\Delta\tau$ was statistically significant (p -value <0.001), the percentage of FRET (E) was calculated as follows: $E = \Delta\tau / \tau$ A488 and fluorochrome interaction was attested by E values > 3 -5% (Camborde et al., 2017). The distance (r) between the donor (A488) and acceptor (A555) was calculated resolving the following equation $E = 1/1+(r/R_0)^6$ as follows:

$$r = [((1/E)-1) \times R_0^6]^{1/6}$$

R_0 (Förster radius) represents the distance at which fluorescence resonance energy transfer from the donor dye to the acceptor dye is 50% efficient ($R_0=7$ nm for A488/A555 according to <https://www.thermofisher.com/fr/fr/home/references/molecular-probes-the-handbook/tables/r0-values-for-some-alex-fluor-dyes.html>).

Transmission electron microscopy (TEM) immunogold and cytochemical labeling:

Ultrathin sections (100 nm) disposed on 200 mesh-copper grids were observed using a HT7700 TEM (Hitachi) (Hitachi, www.hitachi-hightech.com) operated at 80 kV with a Gatan numeric camera (www.gatan.com). False-colors highlighting the three types of walls were added using Corel Photo-Paint on region of interest based on different electron density.

QUANTIFICATION AND STATISTICAL ANALYSIS

RNA isolation and transcript analysis by RT-PCR

Figure S1A: Three experiments were carried out with consistent results. The results are presented as Mean \pm SD; $n = 3$.

Sequence analysis, homology modeling and binding simulation

Figures S5C-E, S6F-G: For each of the five hexagalacturonate tested, the 9 docking position models were superimposed on PRX36 structural model (C) and the corresponding energy values were heat mapped in red-to-yellow (D). The same red-to-yellow color coding was used to label the individual hexagalacturonates (C).

Seed mucilage release phenotyping

Figure 6D-F: Following ruthenium red staining of *A. thaliana* lines complemented with various PRX-TagRFP constructs, scanned images were analyzed with ImageJ (<https://imagej.nih.gov/ij/>) using the above described .txt macro command in order to measure various phenotypical parameters at high-throughput. The mucilage area (μm^2) and the mucilage circularity (0-1 range) were retained as representative parameters for phenotyping. Data was analyzed using Microsoft Excel and statistical Student's t tests were run as compared to Col-0 using the R package (<https://www.r-project.org/>). The Figure 6 was assembled using Corel Photo-Paint. The results expressed as mean values \pm SEM of two independent repeats with a total n = 199-326 seeds are displayed with the *p*-values on the figure. The mean values are color coded using a yellow-to-red heatmap reproducing the RGB colors of the color-coded heat maps generated with Microsoft Excel.

CIII PRX activity measurement

Figure S7: The results are the mean of ≥ 4 replicates \pm SD. Results were analyzed by one-way ANOVA followed by Tukey's significance test; ****P* < 0.0001.

Microscopy observation

All microscopy images: No individual treatment of images was performed to enable comparison between patterns/intensities.

Figure 2: Semi-quantitative analysis was performed by superimposing the trans-cellular fluorescence profiles of 20 cells for each condition.

Figures 4, 5, S2, S3, S4: These images are representative of numerous observations (n >50 MSCs).

Figure 5B, S4C, F, I: The experiment in Figure 5 was repeated thrice independently. In the case of a Gaussian distribution of the individual measured A488 lifetime values (n =30), the

statistical significance of $\Delta\tau = \tau_{A488} - \tau_{A488.A555}$ was assessed with a student's T test. When $\Delta\tau$ was statistically significant (p -value < 0.001), $\Delta\tau$ was used to calculate the Förster distance (d) between the immunocomplexes (see METHODS DETAILS). The mean $\tau \pm$ SEM, $n = 30$ are displayed on the Figure.

Figures 3, 6C-F: Three independent genetic lines were transformed with each constructs: All images are representative of 2-3 observations of > 5 seeds. In Figure 3, only one out of three genetic lines is displayed for each construct and semi-quantitative analysis of the MSC fluorescence profile taken at 12 DAP for 5 cells from three independent transformed lines (black, red, blue lines, respectively) is displayed for each of the four genetic backgrounds. In Figure 6, representative images of the three genetic lines are displayed for each construct.

DATA AND SOFTWARE AVAILABILITY

Not relevant for this study

ADDITIONAL RESOURCES

Not relevant for this study

KEY RESOURCES TABLE (see specific file submitted separately)

SUPPLEMENTAL INFORMATION

Figure S1. Time course of *PRX36* and *PMEI6* expression in developing siliques and of *PRX36* epitope accumulation in *A. thaliana* developing seeds, Related to Figure 1.

Figure S2. Double immunofluorescence labeling specificity, Related to Figures 4, 5, S3 and S4.

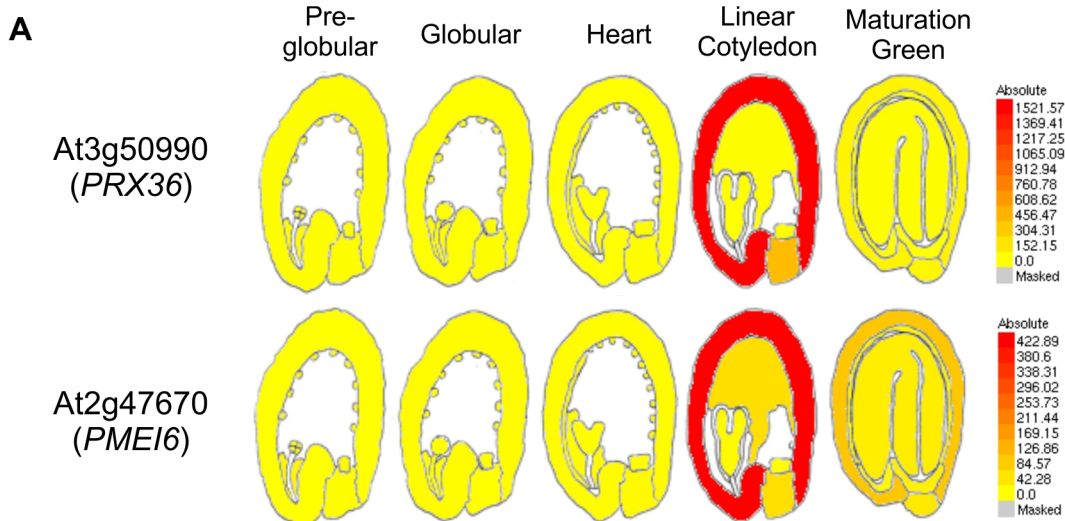
Figure S3. The stable immunofluorescence labeling of *PRX36* to the outer cell wall domain of seed MSCs necessitates the co-localization of partially methylesterified HG *JIM7* epitopes, Related to Figure 4.

Figure S4: FRET- FLIM immunofluorescence demonstrates that co-localized *JIM7* and *CBM3a* immunocomplexes are in 10 nm vicinity, Related to Figure 5.

Figure S5. *in silico* PRX36 structural modeling and PRX36-pectin docking assays identify a putative docking valley on PRX36 with higher affinity for JIM7-specific partially methylesterified hexagalacturonates, Related to Figures 6 and S6.

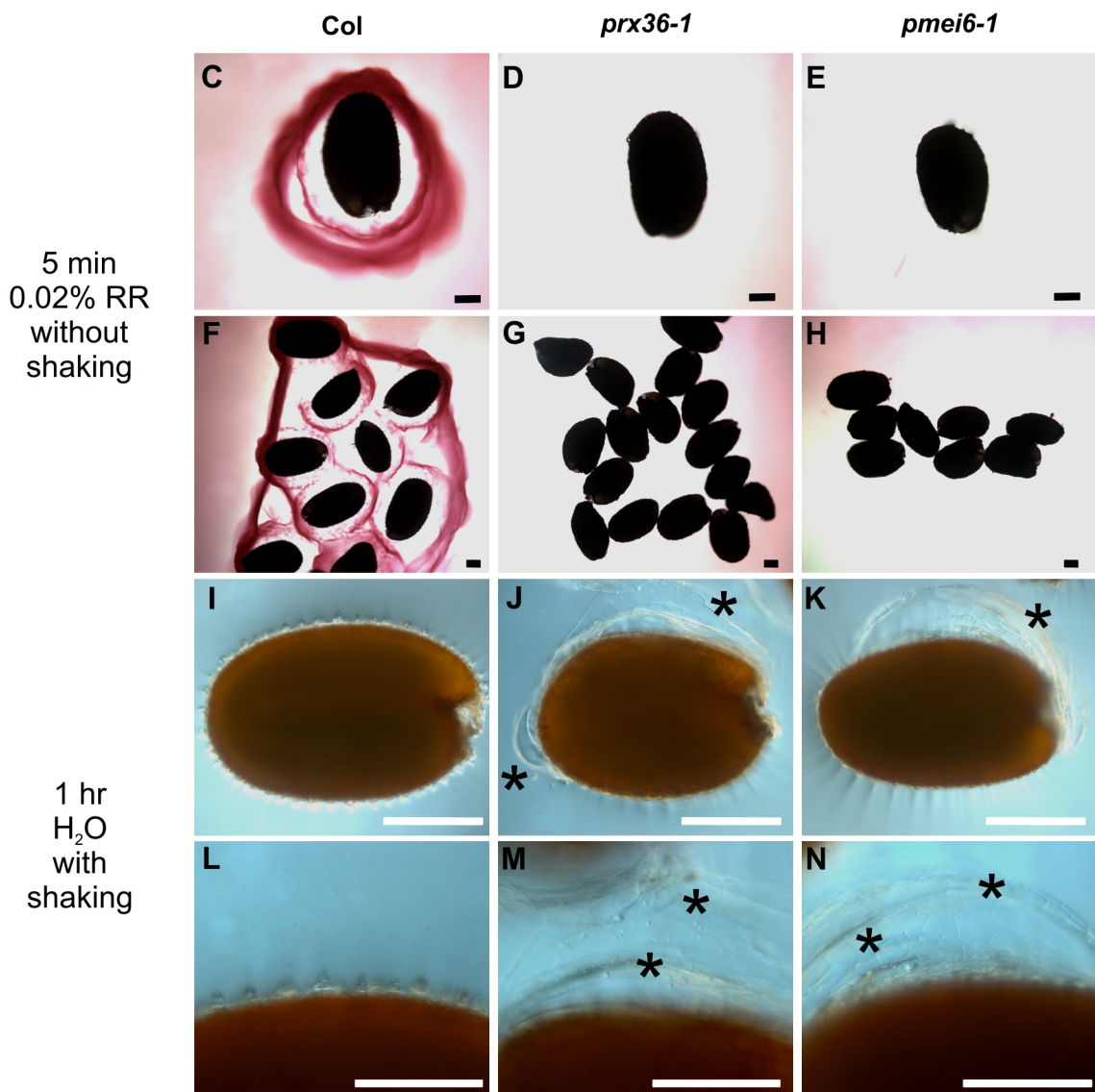
Figure S6. *in silico* PRX36-pectin docking assays identify putative specific amino acids within the predicted hexagalacturonate docking valley, Related to Figures 6 and S5.

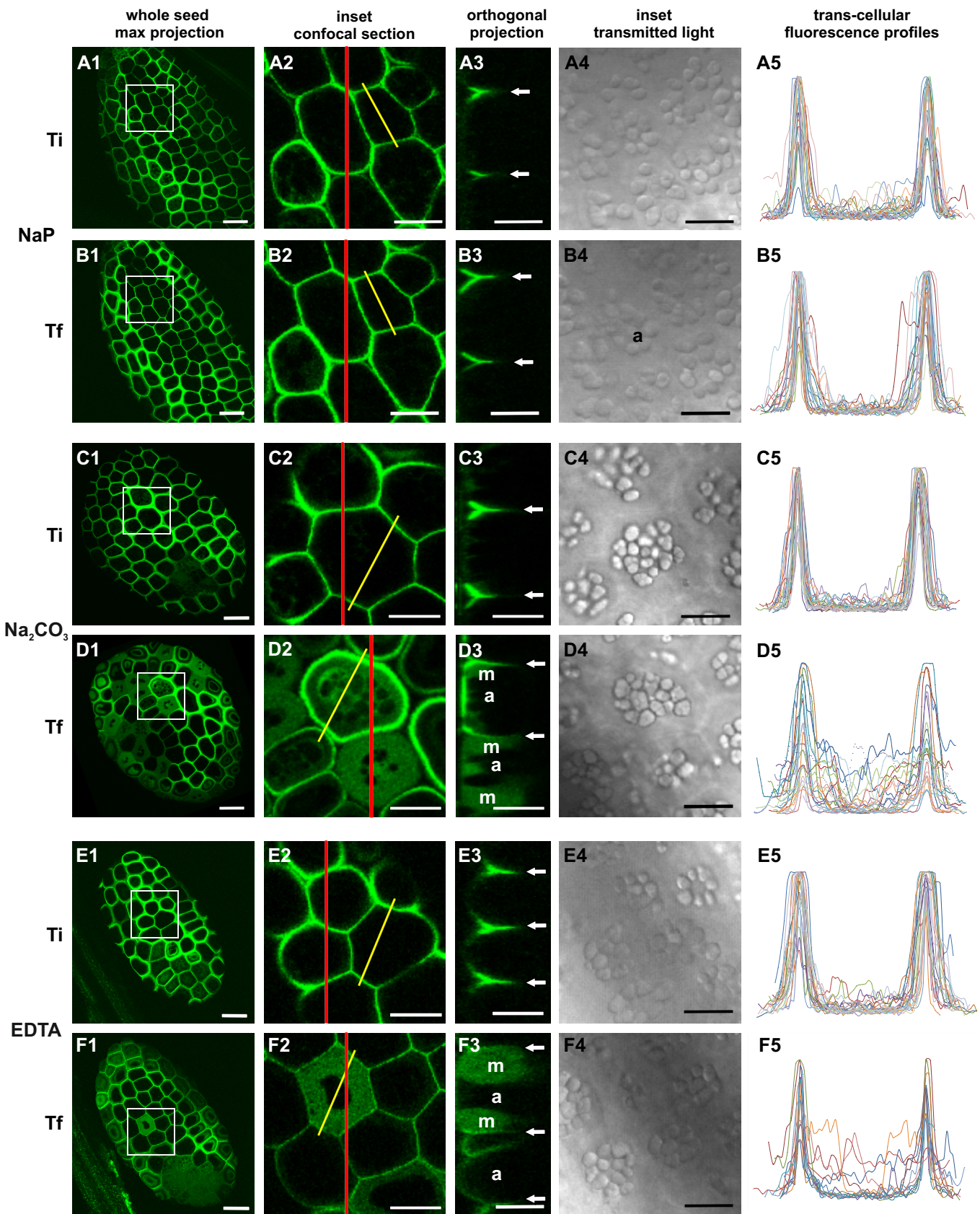
Figure S7. Subcellular localization and CIII PRX activity measurement of PRX36-TagRFP and PRX36m-TagRFP transiently overexpressed in *N. benthamiana*, Related to Figure 6.

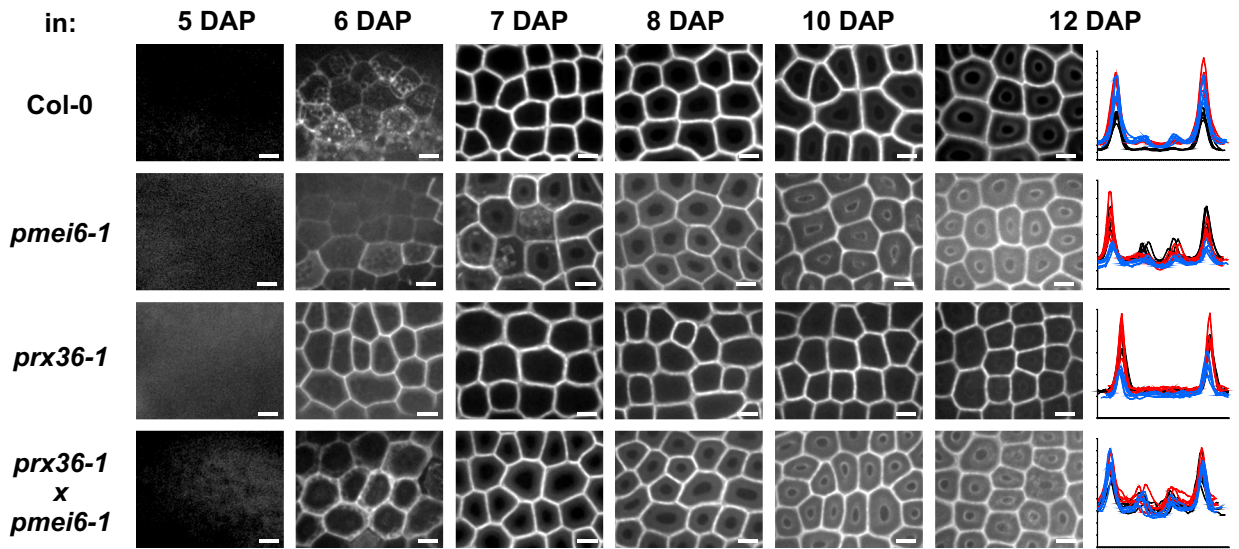
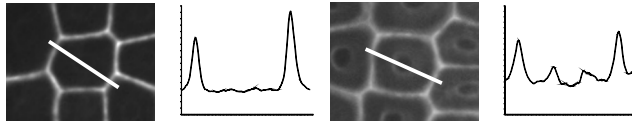


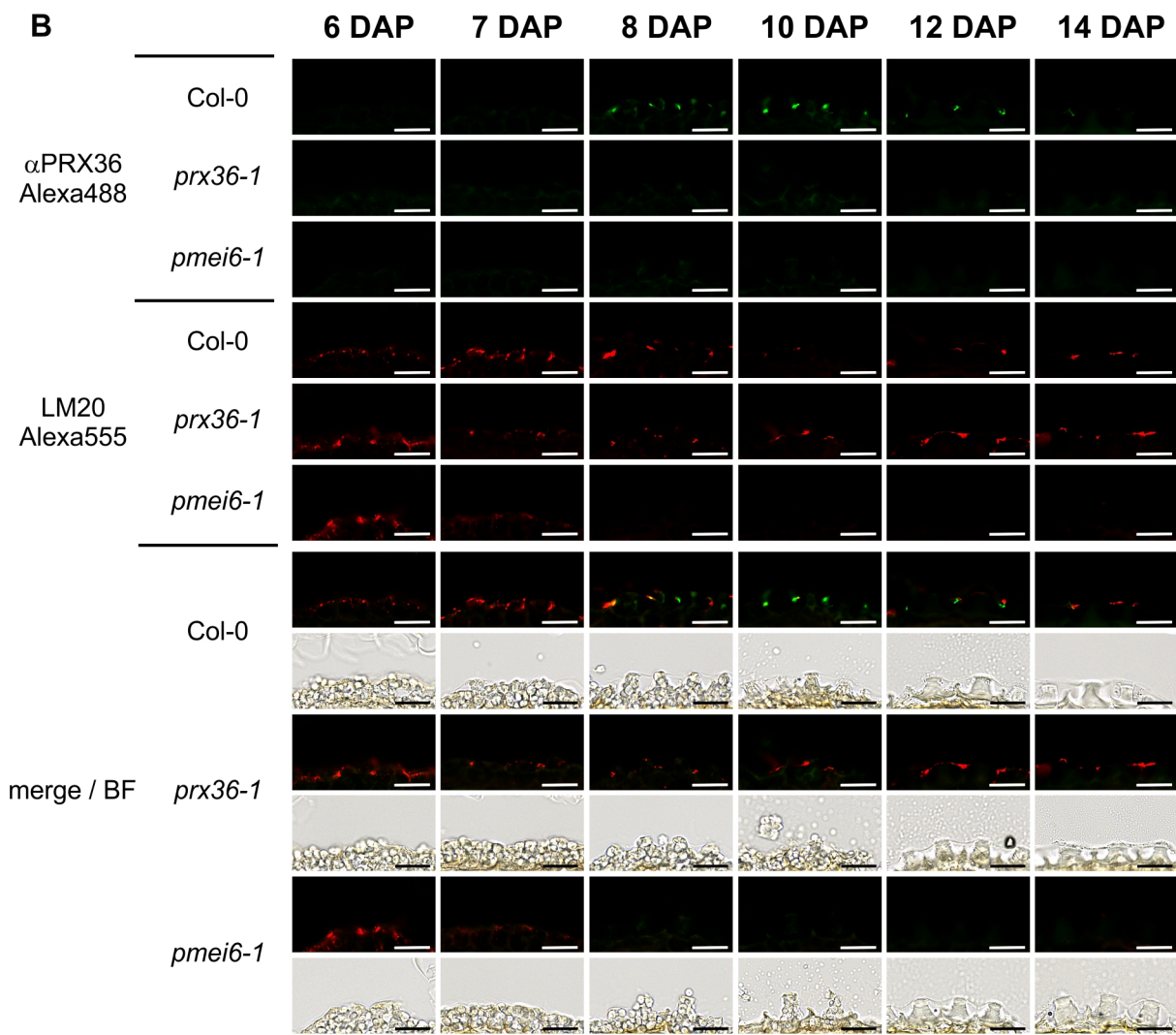
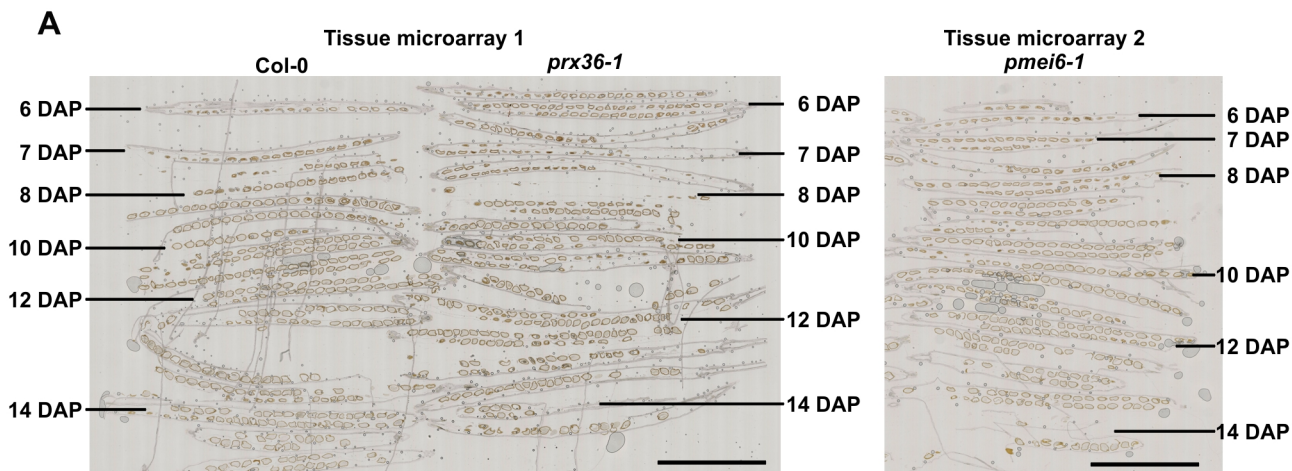
B

RK	PCC	ORF/AGI	pre-globular stage										globular stage										heart stage										linear-cotyledon stage										bending cotyledon stage										mature green stage									
			pg EP	pg MC	pg PEN	pg CZ	pg EN	pg SC	pg WS	g EP	g SUS	g MC	g PEN	g CZ	g EN	g SC	g WS	h EP	h MC	h PEN	h CZ	h EN	h SC	h WS	lc EP	lc MC	lc PEN	lc CZ	lc EN	lc SC	lc WS	bc EP	bc MC	bc PEN	bc CZ	bc EN	bc SC	bc WS	mg EP	mg MC	mg PEN	mg CZ	mg EN	mg SC	mg WS																	
1		1 <i>PRX36</i>	15	27	4	11	8	8	2	4	2	13	2	12	8	2	4	3	3	3	15	14	3	9	4	5	9	12	405	1522	554	1	2	27	992	29	20	7	1	11	3	53	65	9																		
2	0.9474	<i>PME16</i>	2	15	7	8	2	1	6	2	1	2	1	2	2	6	6	2	8	8	4	10	6	13	10	54	54	1	52	423	236	6	34	14	232	65	52	29	11	19	25	37	93	34																		

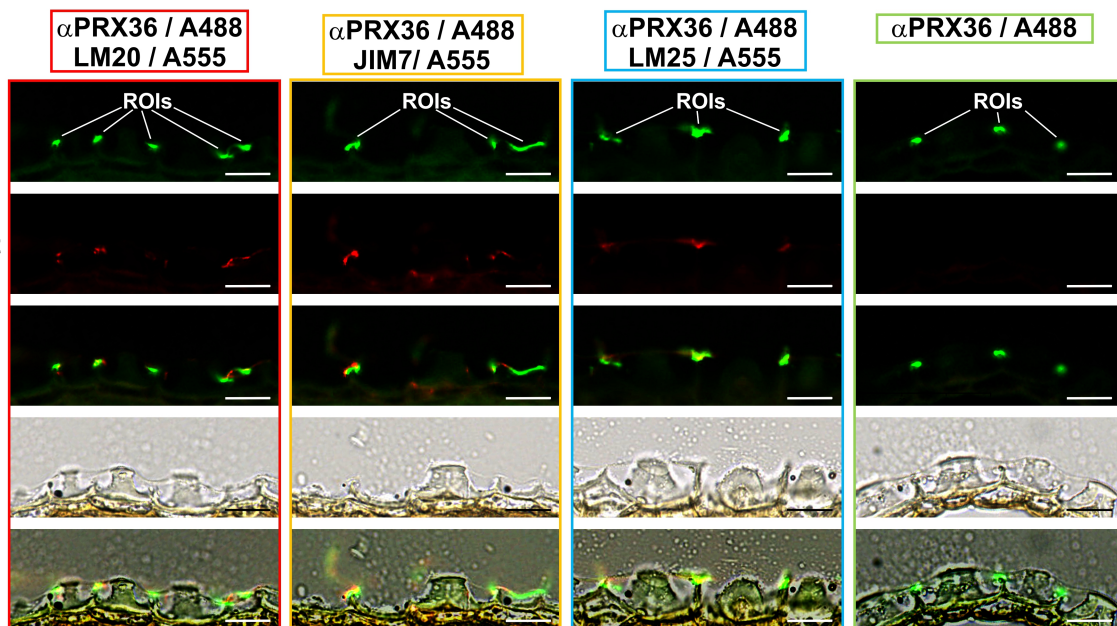




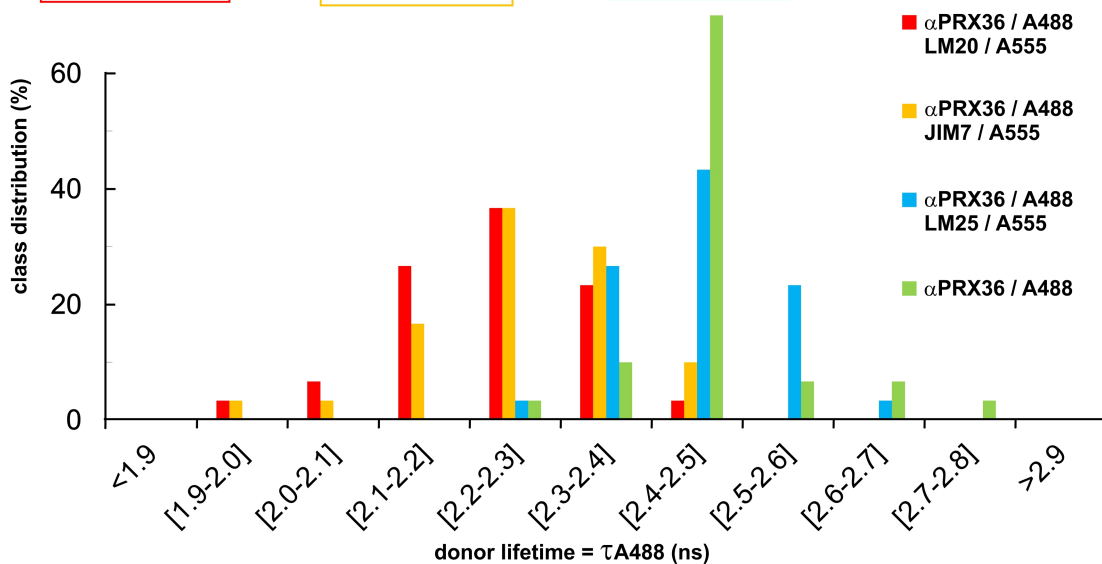
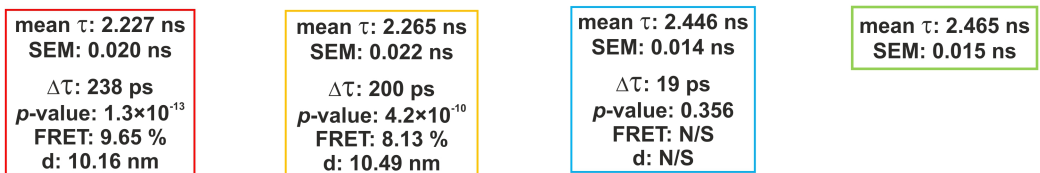
A**proPRX36:
PRX36-
TagRFP****B**

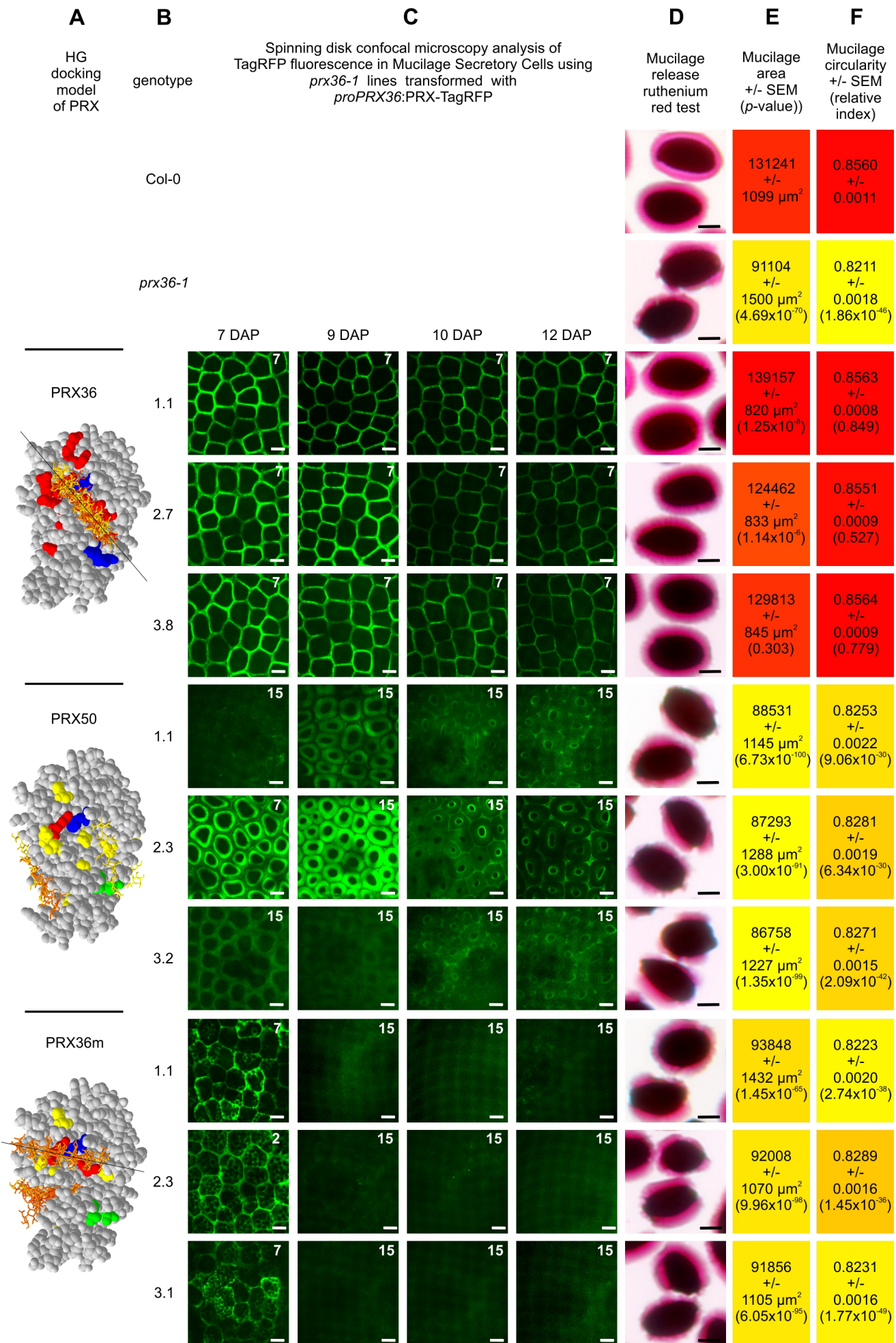


A

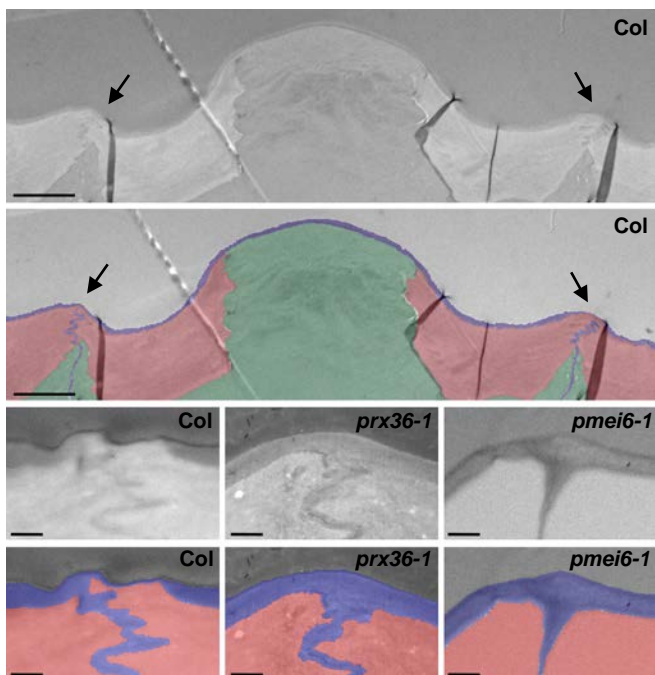


B

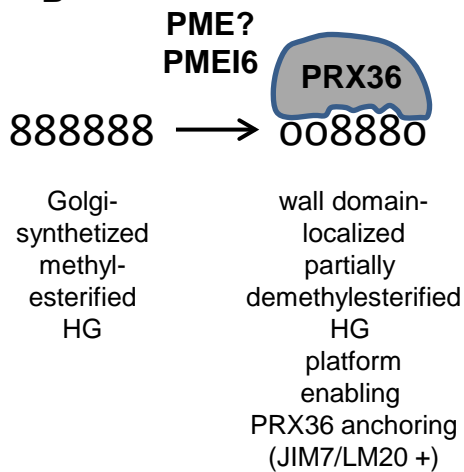




A



B



C

